# A Microdot Multilayer Oxide Device: Let Us Tune the Strain-Ionic Transport Interaction

Sebastian Schweiger,* Markus Kubicek, Felix Messerschmitt, Christoph Murer, and Jennifer L. M. Rupp

Electrochemical Materials, Department of Materials, ETH Zurich, 8093 Zurich, Switzerland

ABSTRACT   In this paper, we present a strategy to use interfacial strain in multilayer heterostructures to tune their resistive response and ionic transport as active component in an oxide-based multilayer microdot device on chip. For this, fabrication of strained multilayer microdot devices with sideways attached electrodes is reported with the material system $Gd_{0.1}Ce_{0.9}O_{2-\delta}/Er_2O_3$. The fast ionic conducting $Gd_{0.1}Ce_{0.9}O_{2-\delta}$ single layers are altered in lattice strain by the electrically insulating erbia phases of a microdot. The strain activated volume of the $Gd_{0.1}Ce_{0.9}O_{2-\delta}$ is investigated by
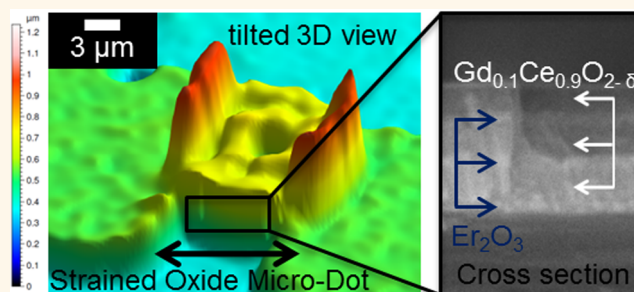
changing the number of individual layers from 1 to 60 while keeping the microdot at a constant thickness; *i.e.*, the proportion of strained volume was systematically varied. Electrical measurements showed that the activation energy of the devices could be altered by $\triangle 0.31$ eV by changing the compressive strain of a microdot ceria-based phase by more than 1.16%. The electrical conductivity data is analyzed and interpreted with a strain volume model and defect thermodynamics. Additionally, an equivalent circuit model is presented for sideways contacted multilayer microdots. We give a proof-of-concept for microdot contacting to capture real strain-ionic transport effects and reveal that for classic top-electrode contacting the effect is nil, highlighting the need for sideways electric contacting on a nanoscopic scale. The near order ionic transport interaction is supported by Raman spectroscopy measurements. These were conducted and analyzed together with fully relaxed single thin film samples. Strain states are described relative to the strain activated volumes of $Gd_{0.1}Ce_{0.9}O_{2-\delta}$ in the microdot multilayer. These findings reveal that strain engineering in microfabricated devices allows altering the ionic conduction over a wide range beyond classic doping strategies for single films. The reported fabrication route and concept of strained multilayer microdots is a promising path for applying strained multilayer oxides as active new building blocks relevant for a broad range of microelectrochemical devices, *e.g.*, resistive switching memory prototypes, resistive or electrochemical sensors, or as active catalytic solid state surface components for microfuel cells or all-solid-state batteries.

KEYWORDS: microdot · strain · conductivity · metal oxide · ceria · microdevice · thin film · resistive switching · erbia · Raman · memristor

Lattice strain engineering is being discussed as a new route for tuning material and device properties in metal oxide films through the manipulation of mass and charge transport. Such films could be employed to improve contemporary metal oxide based devices for next generation energy storage and conversion or for new memristive memory and logic devices. For example, the field of nanoionics considers the fabrication and control of ionic and electronic migration by internal interfaces in heterostructures as a promising alternative to classic doping in metal oxides. This is realized by thin film heterostructures where a conventional metal

oxide is replaced by repetitions of two oxide materials of varying electrical transport and band structure characteristics. At each oxide film's interface variations in the interatomic distances, space charge, and local chemistry result. Since these are artificial thin film structures, size effects (defined by the total volume of the strained or space charged interface regions) provide a new degree of freedom in tuning the resistive and capacitive contributions. The range through which these parameters can be varied is also far broader than can be achieved for a single metal oxide; in particular because of the difference in the electronic structure at the interface which influences all mobile

defects, namely electrons, holes, oxygen vacancies and ions. Classic examples of purely ionic (or mixed ionic electronic) conducting heterostructures are metal oxide films composed of an insulating metal oxide such as $SrTiO_3$, Al_2O_3, or RE_2O_3 with RE=Y, Sc or Lu, and an ionic conductor such as doped CeO_2 or ZrO_2.[1−6] The total ionic conductivity, which predominantly originates from the small band gap oxide phase (*i.e.*, the ceria or zirconia-based phase), depends on the ionic defect migration and association energies and its oxygen vacancy concentration. These can be actively tuned through the imposed compressive or tensile strain of the insulating phase on the ionic conducting phase. Local variations in the near cationic−anionic order such as changed bond strengths as well as bond breaking and reformation may happen at a strained interface.

The first computational studies revealed that strain at interfaces influences the migration energy barrier for oxygen diffusion.[7−9] First experiments by Sata[10] gave a proof-of-concept for conductivity engineering using artificial BaF_2/CaF_2 heterostructures. Azad *et al.*[1] showed an increase in the ionic conductivity of 1 order of magnitude for gadolinia-doped ceria/zirconia heterostructures with an increasing number of interfaces from 2 to 16 at a constant film thickness (for 350 °C). This was confirmed by a recent study of Sanna[11] reporting a 1 order of magnitude increase in ionic conductivity and a decrease in activation energy by Δ0.33 eV when increasing the number of interfaces from 1 to 19 at constant total film thickness. Garcia-Barriocanal even reported a strong increase of conductivity by 8 orders of magnitude for the heterostructure $SrTiO_3$/Yttria-stabilized Zirconia (YSZ).[6] This work triggered great interest in the field; however, the results have been debated.[12,13] Yildiz[13] and De Souza[14,15] concluded from computational results that the increase of conductivity due to strain in a $SrTiO_3$/YSZ heterostructure reaches a theoretical limit at 3 to 4 orders of magnitude. Systematic manipulation of compressive *vs* tensile strain imposed on conducting YSZ phases for heterostructures composed of the materials Y_2O_3/YSZ, Ca-stabilized-Zirconia/Al_2O_3, Sc_2O_3/YSZ and Lu_2O_3/YSZ was thoroughly investigated in model experiments by Janek, Korte and co-workers.[2−5,16,17] It was reported that variation of the lattice misfits up to 3% tensile strain acting on the YSZ phase of the heterostructure substantially increased ionic conductivity, whereas the opposite trend (a respective decrease of conductivity) was measurable for −4% of compressive strain.

It can be concluded that several reports highlight the potential to change the transport properties in ionic-conducting heterostructures over a broader range when compared to single constituent materials. It is important to note that classic extrinsic doping in ionic conductors hardly modifies the overall ionic conductivity of zirconia or ceria by more than 1 to 2 orders of magnitude; for details see Rupp[18,19] and Omar.[20] Despite the promises of the first results the fundamental issue is how much the ionic conductivity of a fluorite-type oxide can be altered through lattice strain in a heterostructure. The hope for a new generation of electrochemical microdevices stems from the ability to manipulate the strain-ionic transport interaction in metal oxide heterostructures. Nevertheless, up to now electrochemical microdevices, *e.g.*, fuel cells, sensors, batteries or memristive switches,[21] which use strained metal oxides as functional building blocks, simply do not exist. In order to implement ionic heterostructures in commercial applications, an understanding of the strain-related near order changes and ionic transport are a basic requirement. New microfabrication routes to efficiently access the strain modulated resistive and capacitive volumes of the ionic conducting phases in the heterostructures need to be envisioned for new microdevice prototypes and are discussed throughout this work.

What Is Critical for Electric Contacting Strategies on Ionic Heterostructures? The questions requiring attention in order to implement strained ionic heterostructures as functional materials in microdevices concern both the control over the near order interfacial states and new device fabrication routes to access the strained oxide volume's resistive and capacitive contributions for measurements.

Near Order Interfacial States of Strained Ionic Heterostructures. First, there is a debate on the magnitude of ionic conductivity enhancement for compressively and tensely strained ceria and zirconia phases in heterostructures in literature. In some cases a strong increase is observed, whereas in others no effect is measured for a similarly strained heterostructure oxide material and volume; see Santiso and Burriel[22] or Kilner[13] for details. In this sense, we believe that a critical aspect in comparison of the experimental results is the electrode arrangement and fabrication relative to the strained volume fractions and interfaces of the heterostructure oxides. Conventionally, electrical transport/capacitance is measured in a 2- or 4-point electrode arrangement. Some authors apply the electrodes toward the sides of a grown multilayer on a single crystalline substrate *via* paste and wire macroscopically.[2,23,24] In that case the electric field lines are along the interface (parallel to the internal interfaces). Nevertheless it remains within the uncertainty whether all strained volume fractions of the heterostructure (down to a few nanometers in single layer thicknesses) are effectively contacted by this rather macroscopic contacting method. In other cases electrodes were deposited by metal sputtering on top of the heterostructure.[25−27] It is important to note that here the electrodes are applied parallel to the strained interface. For the case that one heterostructure phase

dominates in fast ionic conduction the electric field lines may be completely restricted to the top single layer and blocked at the insulating phase. Regardless of the effective strain acting on the ionic conducting phase, only the closest ionic conducting single layer to the electrode may contribute to the overall transport, and the biggest fraction of the strained volumes would be missed in its contribution to total conduction.

Second, calculations of strain at the ionic heterostructure interfaces are based on classic long-range cationic structure determination tools like XRD[11] or electron microscopy[28] where anionic lattice positions are calculated but not physically measured. Interestingly, Korte measures inconsistencies in the remaining lattice strain of a single layer with respect to its thickness by XRD.[2] The authors concluded that the effective strained volumes contribute to the total oxygen ionic transport measured; however, structural modulations at the interface could not be resolved by XRD.

Our emphasis is on introduction of Raman spectroscopy as a new tool for systematically investigating changes in anion−cation bond strength with respect to strained volume fractions in ionic heterostructures. The anion−cation bonds are crucial for the ease of oxygen ionic hopping and can even directly be correlated in Raman *via* computational tools, *e.g.*, DFT,[19] to changes in migration and association energies. Recently, Raman studies on strain-transport interaction were reported for single metal oxide films with ionic bonds, *i.e.*, for ceria[19] or $LaCoO_{3-\delta}$.[29] Raman is also commonly used to characterize strain states in covalently bonded semiconductors like Si,[30] GaN,[31] or graphene.[32] However, to the best of our knowledge Raman studies on ionic conducting heterostructures are still missing in the field.

First Electrochemical Microdevices based on Strained Ionic Heterostructures? To date the fundamentals of strained heterostructures have not been elucidated for electrochemical microdevices. In particular, resistive and capacitive contributions could be altered and triggered over broader ranges and carrier diffusivities and device switch times for different states may be accessed over broader ranges than with classic materials. Interestingly, the majority of reports in the field envision heterostructures as new fast conductive electrolyte materials for microsolid oxide fuel cells[22,33,34] operating at intermediate temperatures (∼400 °C). But, if we carefully analyze literature one can conclude that the difference in conductivity and diffusion coefficient modulation with respect to strain substantially increases for decreasing operation temperature of the device (see *e.g.*, ref 14 for a computational study and for experimental evidence refs 2, 5, and 24). Therefore, we shift our focus to the new area of memristive information memories and logics and suggest implementing ionic heterostructures as new building blocks for modulating resistive/capacitive contributions of

the switches through manipulating the interfacial lattice strain (operating at room temperature); see ref 21. Such devices generally consist of a metal/metal oxide/metal structure. It is imperative to operate the resistive switch with electrodes at small distances, since high local electric field strengths (of the order of >10⁶ V/m) are required to observe nonlinear hysteretic current−voltage profiles.[35]

We suggest replacing the current state-of-the-art single phase metal oxide building block with a multilayer heterostructure made of two metal oxides (*A* and *B*) stacked in a repetitive manner (*i.e.*, $A-(B-A)_n-B$) with strained internal interfaces for new types of redox-based resistive switches.[21] The memristive and hysteretic current−voltage characteristics depend on carrier flux. Different resistances can be assigned to binary (or multilevel) states which can be used for digital information storage in new memory devices.[36] Oxide-based resistive switches are a promising alternative to dynamic random-access memory (DRAM) and nonvolatile flash memory used in today's computing and portable data storage devices due to increased nanosecond-speed operation and low write voltages. These resistive switches could also be used as logic devices and even allow for stacking of multiterminal cross-bar arrays which is superior to classic transistor based lateral stack concepts.[37−43] In the present paper strain engineering of oxide multilayers is suggested as new strategy to manipulate the properties of metal oxide films. The first strategies to realize such devices in the microscale are demonstrated and discussed. Through this approach resistive and capacitive properties of the multilayer oxide can be manipulated by far more than with classic doping in single films. For this, the two metal oxides $Gd_{0.1}Ce_{0.9}O_{2-\delta}$ and Er_2O_3 as constituents of the sideways contacted multilayer microdots were selected for implementation as the first future strained resistive switching prototypes. $Gd_{0.1}Ce_{0.9}O_{2-\delta}$ was chosen, since it is a well-studied model material under strain as single phase. In addition, first reports on nonstrained ceria-based resistive memories have been reported.[44−49] One may also highlight that the new structuring concept of the heterostructure microdots may also be implemented in other electrochemical chip devices such as resistive sensors or catalytic active surface electrodes for batteries or fuel cells.

To this end, we develop a microdot device structure for which we establish a new fabrication route to allow for "sideways" and micrometer-scale contacting of strained multilayer $Gd_{0.1}Ce_{0.9}O_{2-\delta}/Er_2O_3$ dots. Unlike traditional means for varying the resistive characteristics of the metal oxide film by doping, we demonstrate in this study that large changes in the resistive characteristics can be obtained by tuning the interfacial multilayer lattice strain of micrometer-sized dots in a microelectrochemical device. Through a variation

of the number of multilayer interfaces and the single layer thickness, compressive strain is imposed on the ionic conducting ceria-based phase by the electrically insulating phase of erbia. Lattice strain states are measured for the $Gd_{0.1}Ce_{0.9}O_{2-\delta}$ and Er_2O_3 layers within the heterostructures conventionally by XRD and also by Raman spectroscopy as a new approach for characterizing the near order *via* bond strength changes down to single layer thickness of several nanometers for heterostructures. We discuss the role of compressive lattice strain, and near order changes with decreasing single layer thicknesses ranging from 275 nm down to 3 nm ($Gd_{0.1}Ce_{0.9}O_{2-\delta}$) and 7 nm ($Er_2O_3$) on ionic conductivity for $Gd_{0.1}Ce_{0.9}O_{2-\delta}$/ Er_2O_3 multilayer oxide dots. Furthermore, we elucidate the importance of the newly proposed contacting strategy at microdistances (*vs* conventional top electrodes) for strained ionic conducting multilayers over the sides of the microdevice. We also give a proof-of-concept for the electrode design to capture real strain effects in transport. This work presents the first strain-resistance modulation characteristics of heterostructure oxide dots in a microdevice on a chip and provides a basis for a new type of resistive switch.

RESULTS AND DISCUSSION

Fabrication of Strained Oxide Microdevices on a Chip. Microscopy images and schematics of the microdevice structures consisting of strained multilayer $Gd_{0.1}Ce_{0.9}O_{2-\delta}$/ Er_2O_3 thin film dots with pairs of sideways Pt contacts arranged in an array are presented in Figure 1. The light microscopy top-view shows the successfully fabricated array of Pt electrode pairs contacting a strained multilayer erbia/gadolinia-doped ceria dot at low magnification (Figure 1a). At higher magnification, a free etched erbia/gadolinia-doped ceria multilayer dot structure is visible as a square shaped area with an edge length of $\sim$15 μm in interference colors arranged between two Pt electrodes (Figure 1b). Laterally resolved Raman spectroscopy was used to verify that the structured multilayer films were completely free-etched dots with no remains on the substrate. For this, the characteristic vibrational modes with respect to the spot on the chip were analyzed as detailed in Supporting Information S1. A requirement of this work is to deposit and shape Pt microelectrode pairs, which allow for electrical contacting of each multilayer film island structure along all of its strained interfaces and at short electrode distances; see schematic in Figure 1c. For this, a regular pattern of Pt electrodes was deposited onto the free-etched multilayer film islands. The Pt electrodes overlap the island so that the metal contacts the multilayer thin film island at its sloping side walls (Figure 1b,d: schematic and 3D optical profiles). An SEM image of the multilayer film's cross sections is shown in Figure 1e. For the image recorded with the backscatter detector the different

single layer phases of the multilayer oxide film can be visualized by their difference in atomic mass. Here, bright contrast refers to the more strongly back-scattered electrons of the heavy erbium-oxide single layers and darker ones to the lighter ceria single layers. The selected multilayers show a thin film with 290 nm in total film thickness and a set of 3 bilayers of $Gd_{0.1}Ce_{0.9}O_{2-\delta}$ and Er_2O_3 (*i.e.*, the number of $Gd_{0.1}Ce_{0.9}O_{2-\delta}$/$Er_2O_3$ interfaces is 5). A single layer thickness of $\sim$35 nm of Er_2O_3 and 62 nm of $Gd_{0.1}Ce_{0.9}O_{2-\delta}$ can be determined from the cross-section and is in good agreement with the intended pulsed laser deposition processing conditions of 32 and 64 nm for Er_2O_3 and $Gd_{0.1}Ce_{0.9}O_{2-\delta}$, respectively. All films deposited throughout the study revealed comparable film thicknesses within an error of $\pm$10% and revealed continuous and dense film microstructures.

In this part, we present a new strategy to prepare sideways contacted multilayer oxide thin film dot arrays to measure along the strained interfaces for small electrode distances of $\leq$15 μm. This differs to classic contacting strategies for ionic conducting and strained multilayer oxides in the sense that top in-plane electrode measurements have been avoided and electrode distances were reduced by more than 2 orders of magnitude.

In the following, the crystallographic structures, near order and bond length (representative of bond strength) and ionic conductivity characteristics of $Gd_{0.1}Ce_{0.9}O_{2-\delta}$/$Er_2O_3$ multilayers and single films are presented as a function of number of interfaces and lattice strain. The role of the interfacial lattice strain and its interaction volume on the ionic conductivity of the fast conducting $Gd_{0.1}Ce_{0.9}O_{2-\delta}$ phase is next investigated for the multilayer dot microdevice structures.

Lattice Structure and Strain State of the $Gd_{0.1}Ce_{0.9}O_{2-\delta}$/$Er_2O_3$ Multilayer Thin Films. The X-ray diffraction patterns of the single Er_2O_3 and $Gd_{0.1}Ce_{0.9}O_{2-\delta}$ films and of $Gd_{0.1}Ce_{0.9}O_{2-\delta}$/$Er_2O_3$ multilayer thin films with a varying number of thin films interfaces from 5 to 59 [($Gd_{0.1}Ce_{0.9}O_{2-\delta}$/$Er_2O_3$) $\times$ 30] are displayed in Figure 2. Detailed information on the XRD scans is available in Supporting Information S2. The diffractograms of the reference single film samples of Er_2O_3 and $Gd_{0.1}Ce_{0.9}O_{2-\delta}$ show single peaks for the first and second order, being the orientations (111) and (222) for $Gd_{0.1}Ce_{0.9}O_{2-\delta}$ and (222) and (444) for Er_2O_3, Figure 2a. The $Gd_{0.1}Ce_{0.9}O_{2-\delta}$ single film reveals a cubic fluorite structure with a measured lattice parameter of 0.5430 nm, Figure 2b. The (111) orientations observed for the $Gd_{0.1}Ce_{0.9}O_{2-\delta}$ films are in agreement with literature.[50,51] A cubic bixbyite structure with a lattice parameter of 1.061 nm was determined for the Er_2O_3 single film. The single film phases and structure types agree with own processed and measured reference ceramic pellets (see Supporting Information S3). Further, this is in agreement with literature; see for
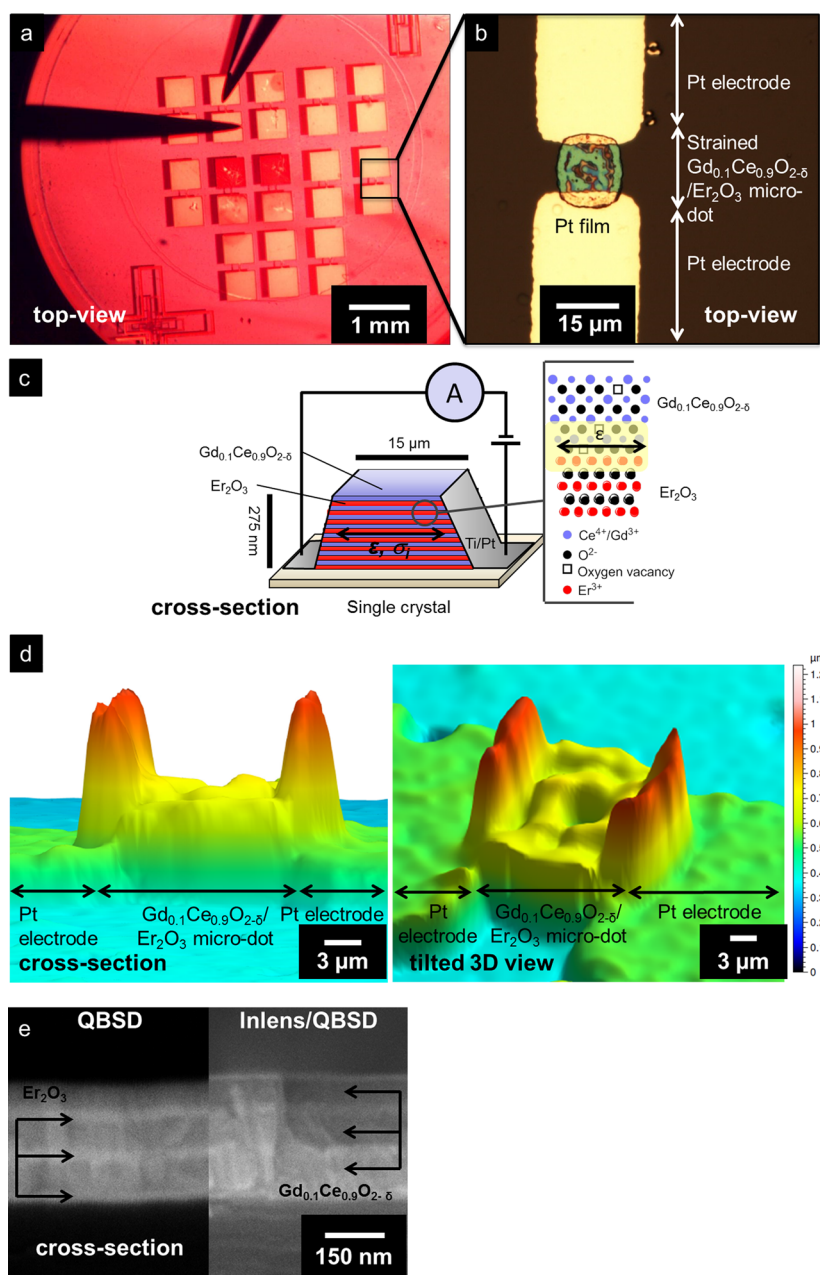
Figure 1. Microscope view-graphs of strained $Gd_{0.1}Ce_{0.9}O_{2-\delta}$/$Er_2O_3$ multilayer microdots and arrays on chip. (a) Top view low magnification light microscopy image of an electrode array contacting sideways islands of $Gd_{0.1}Ce_{0.9}O_{2-\delta}$/$Er_2O_3$ multilayer microdots on chip. Tungsten needles were used for electrical contacting of the Pt-side contacts. (b) High magnification light microscopy image of Pt electrodes contacting a structured multilayer thin film dot (top view). (c) Schematic view graphic of a strained multilayer $Gd_{0.1}Ce_{0.9}O_{2-\delta}$/$Er_2O_3$ heterostructure. The electrodes that are attached to the side walls of the structure allow measuring the conductivity parallel to the strained $Gd_{0.1}Ce_{0.9}O_{2-\delta}$/$Er_2O_3$ interfaces. (d) Side view and tilted 3D view for a microdot arranged between two metal electrodes by optical surface profilometry. Here, the scale bar refers to the horizontal width (aspect ratio is not to scale). The color bar indicates the measured heights. (e) SEM cross-sectional view of a $Gd_{0.1}Ce_{0.9}O_{2-\delta}$/$Er_2O_3$ multilayer in a microdot. The left side shows a QBSD image and the right side shows a 50% QBSD and 50% In-lens detector image. In the QBSD image the bright contrast phase refers to the Er_2O_3 (heavy mass) and the dark one to the $Gd_{0.1}Ce_{0.9}O_{2-\delta}$ (light mass).

details on $Gd_{0.1}Ce_{0.9}O_{2-\delta}$ refs 20 and 52 and for Er_2O_3 ref 53. It can be concluded that the two materials grow in a 1:2 commensurability in lateral view: the orientation of the (0001) sapphire imposes biaxial texture on the single film compounds. The XRD patterns of the single films are compared to multilayer films of $Gd_{0.1}Ce_{0.9}O_{2-\delta}$/$Er_2O_3$ with varying numbers of interfaces from 5 to 59 and a decreasing single layer thickness from 280 to 7 nm (255 to 3 nm for Er_2O_3). The total thickness of the multilayers was kept constant at approximately 275 nm. All multilayer thin films show the (111) $Gd_{0.1}Ce_{0.9}O_{2-\delta}$ and (222) Er_2O_3 signature peaks as well as their higher orders. Hence, a successful orientation and biaxial texturing of the individual
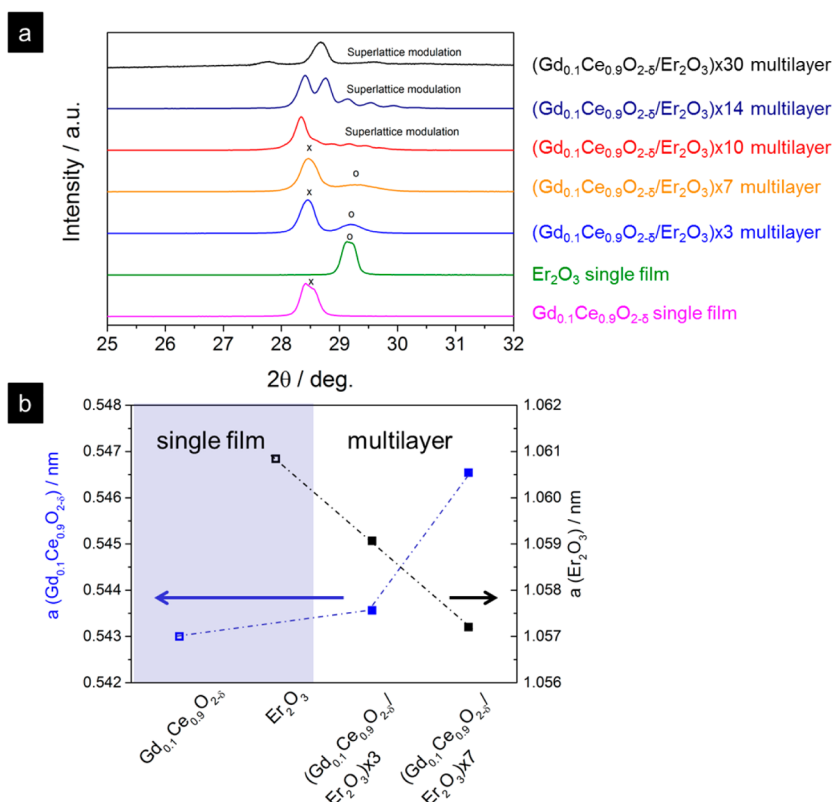
Figure 2. XRD measurements of the Er_2O_3 and $Gd_{0.1}Ce_{0.9}O_{2-\delta}$ single thin films and multilayer thin films. (a) The diffractograms show clearly crystalline and textured thin films. The samples with high number of interfaces, 10 to 30 bilayers (19 to 59 $Gd_{0.1}Ce_{0.9}O_{2-\delta}/Er_2O_3$ interfaces), show additional satellite peaks, indicating superlattice modulation. The sign (x) refers to $Gd_{0.1}Ce_{0.9}O_{2-\delta}$[52] and the sign (o) refers to Er_2O_3.[53] (b) Comparison of the out-of-plane lattice parameters with respect to the number of interfaces for the $Gd_{0.1}Ce_{0.9}O_{2-\delta}$ and Er_2O_3 single films and the multilayer thin films for ($Gd_{0.1}Ce_{0.9}O_{2-\delta}/Er_2O_3$) × 3 and ($Gd_{0.1}Ce_{0.9}O_{2-\delta}/Er_2O_3$) × 7. Total film thickness was kept constant at 275 nm.

single layers in the multilayer toward the (0001) sapphire substrate can be concluded. We observe this independent on the number of interfaces and down to a single layer thickness of 18 nm. On the basis of the diffraction data in growth direction we conclude that the best match for the multilayer growth of the thin film materials is realized in the [111] and [222] orientation for $Gd_{0.1}Ce_{0.9}O_{2-\delta}$ and Er_2O_3 according to the trifold symmetry of the (0001) plane of the sapphire substrates. Hence, out of geometrical considerations the trifold symmetry of the (111) plane of Er_2O_3 should correspond to the best match with the trifold symmetry with a 4:3 lattice spacing commensurability in the multilayer.

In general, we observe systematic shifts of the (111) $Gd_{0.1}Ce_{0.9}O_{2-\delta}$ peak toward lower and for the (222) Er_2O_3 peak toward higher diffraction angle with increasing number of multilayer interfaces from 5 to 13. For higher numbers of multilayer interfaces, erbia and gadolinia-doped ceria (111) and (222) peaks overlap as the shifting progresses (respectively for single layer thicknesses 18 nm), Figure 2a. We interpret this as characteristic features of superlattices with the mean structure peaks surrounded by satellite peaks, in agreement with refs 54 and 55. Similar observations have

been made in earlier studies on ionic heterostructures of ceria/8 mol % yttria-stabilized zirconia by Pergolesi[25] for single layer thicknesses of 9 nm. The angular positions of the satellite peaks were used to calculate the bilayer thickness, according to the following equation:[25]

$$\Lambda = \lambda/(\sin_{\theta+1} - \sin_{\theta-1}) \qquad (1)$$

where Λ is the bilayer thickness and $\sin_{\theta+1}$ and $\sin_{\theta-1}$ are the positions of the first-order satellite peaks of the superlattice. The resulting $Gd_{0.1}Ce_{0.9}O_{2-\delta}/Er_2O_3$ bilayer thickness is $\Lambda_{Gd_{0.1}Ce_{0.9}O_{2-\delta}/Er_2O_3} = 10$ nm, which is in very good agreement with the profilometer measurements.

In Figure 2b the out-of-plane lattice constants calculated out of clearly resolved Bragg reflections of the multilayers with 5 to 13 interfaces are shown. The lattice constant of $Gd_{0.1}Ce_{0.9}O_{2-\delta}$ is increased as the thickness of the individual layers is decreased, while the lattice constant of Er_2O_3 is decreased for a decreasing thickness of the individual layers. The values of these out-of-plane lattice constants are in good agreement with the lattice constants reported in literature.[56,57] The out-of-plane lattice constants show an expansion of the lattice for $Gd_{0.1}Ce_{0.9}O_{2-\delta}$ and a compression of the Er_2O_3 lattice, and reverse behavior can be expected for the in-plane lattice strain.

This means it can be expected that the unit cells relax the strain that is imposed on them along the in-plane-direction in the out-of-plane-direction.[58]

Implications of the Lattice Strain on Cationic−Anionic Near Order in the Multilayers. We investigated the near order and bond strength characteristics of the single films and multilayers *via* Raman spectroscopy. This allows direct probing of the Ce−O bond and is therefore very sensitive to changes in the bonding environment. Literature review shows that for the case of Er_2O_3 data is available on single crystalline material;[59,60] however, reports on thin film erbia are missing. More data is available for $Gd_{0.1}Ce_{0.9}O_{2−\delta}$ pellets. Nevertheless reports on thin films are still scarce.[19,61,62] First work on the implication of lattice strain on the gadolinia-doped ceria Raman near order has been recently published.[19] Very recently, Kreisel[63] reported the use of Raman spectroscopy as a probing tool to characterize the strain states of four oxide films for varying penetration depth. It is surprising that Raman near order-strain studies are still lacking for thin films based on metal oxides, despite their established use for covalently bonded materials under strain.[31,32] In Figure 3, spectra for the single thin films and $Gd_{0.1}Ce_{0.9}O_{2−\delta}/Er_2O_3$ multilayers are displayed. The reader is referred to Table 1 for Raman mode assignments.

Single film spectra reveal the following characteristics: The spectrum of the $Gd_{0.1}Ce_{0.9}O_{2−\delta}$ single film sample shows one single peak at about 463 cm^{-1}, Figure 3a. This peak can be assigned to the F_{2g} mode in accordance to literature on similar materials processed as macrocrystalline ceramics. This is further consistent with recent reports on Raman characteristics of $Gd_{0.2}Ce_{0.8}O_{2−\delta}$ PLD thin films.[19,64,65] The spectrum of the Er_2O_3 single thin film reveals 8 measurable Raman active modes. Latter Raman peaks can clearly be assigned to the coupled $F_g + A_g$ and F_g modes[60] of erbia and other rare earth bixbyite structures (Sm_2O_3, Dy_2O_3, Mn_2O_3, Sc_2O_3, In_2O_3),[66] Figure 3a and Table 1. We also compare and confirm through own macrocrystalline doped ceramic standards the assigned peaks for the single thin films (Supporting Information S4). Both single thin film samples, erbia and doped ceria, show additional peaks assigned as "s" originating from the sapphire substrate.

Multilayer $Gd_{0.1}Ce_{0.9}O_{2−\delta}/Er_2O_3$ films are also displayed relative to their number of interfaces for their Raman characteristics in Figure 3a. All multilayers investigated exhibited additional peaks compared to the single films. However, all multilayer spectra are very similar to the same number of peaks independent of the number of single layers. Therefore, relative changes between these spectra were investigated in detail.

A peak at about 455 cm^{-1} can be observed that could be the F_{2g} mode of the $Gd_{0.1}Ce_{0.9}O_{2−\delta}$ component. All other peaks (at higher wavenumbers, *i.e.*, > 460 cm^{-1}) are tentatively assigned to the F_g or other modes of the Er_2O_3 phase. The peak at ∼500 to

∼510 cm^{-1} appears to be a double peak as observable in earlier studies on strained GaN,[31] which is attributed to strain- or orientation-induced mode splitting. However, the peaks are broadened (fwhm$_{singlefilm}$ = 28 cm^{-1}) due the nanocrystalline morphology of the films, and so it remains unclear exactly how many lines are in the region ranging from ∼400 to 600 cm^{-1} and to which Raman modes they correspond. Furthermore, the modes of the sub-10 nm layers are likely shifted due to phonon confinement effects. Therefore, direct comparison of the peak position of the single film and multilayer spectra is not possible without extensive simulations. However, from careful analysis of the multilayer sample Raman spectra we can observe a systematic trend within the multilayer samples. To obtain the superposed Raman peak signatures of the multilayers, we apply Gaussian fit algorithms. The fit of the superposed Raman signatures is exemplarily shown for a sample of the 19 interfaces $Gd_{0.1}Ce_{0.9}O_{2−\delta}/Er_2O_3$ multilayer sample (Figure 3b). For the peak fitting algorithm the peak width was left as a free parameter due to the fact that peaks of different materials and morphologies were fitted and that the peaks could not be assigned beyond doubt. A schematic of the measurement principle is shown in Figure 3c. Here, the principles of XRD and Raman are compared and related to the state at the interface and lattice strain tensor components measured. Dilatational lattice strain can act in three directions of space, denoted ε_{11}, ε_{22} and ε_{33}. The vectors ε_{11} and ε_{22} form the plane along the multilayer interface of the two adjacent materials with ε_{33} as the out-of-plane component being perpendicular to it. Using Raman confocal microscopy in first approximation the direction parallel to the incident beam is measured (neglecting crystal orientation, the numerical aperture of the objective and the refractive index of the sample). In the backscatter configuration the incident excitation beam is perpendicular to the surface, and hence, in a cubic crystal with $\varepsilon_{33} \parallel$ (001) the measured direction is directly proportional to the ε_{33} direction (Figure 3c). However, in the generalized case Raman spectroscopy is sensitive to all modes with eigenvector components parallel to the beam, which are related to in-plane strain components *via* the out-of-plane component ε_{33} and the stiffness tensor c_{ij}. In the present work, the (111) out-of-plane texture invokes a mixing of modes with out-of-plane components. Consequently, a mode splitting would be expected, but due to the broad line-width of our films, the resulting spectra rather show an additional broadening and shift due to strain.[67] The overall shift of the assigned F_{2g} line is recorded by fitting and qualitatively interpreted as strain shift.

The same strain tensor component (ε_{33}) is accessed for XRD in Bragg−Brentano configuration. In Figure 3d we summarize the change of Raman shift within the $Gd_{0.1}Ce_{0.9}O_{2−\delta}/Er_2O_3$ multilayer samples. The peaks
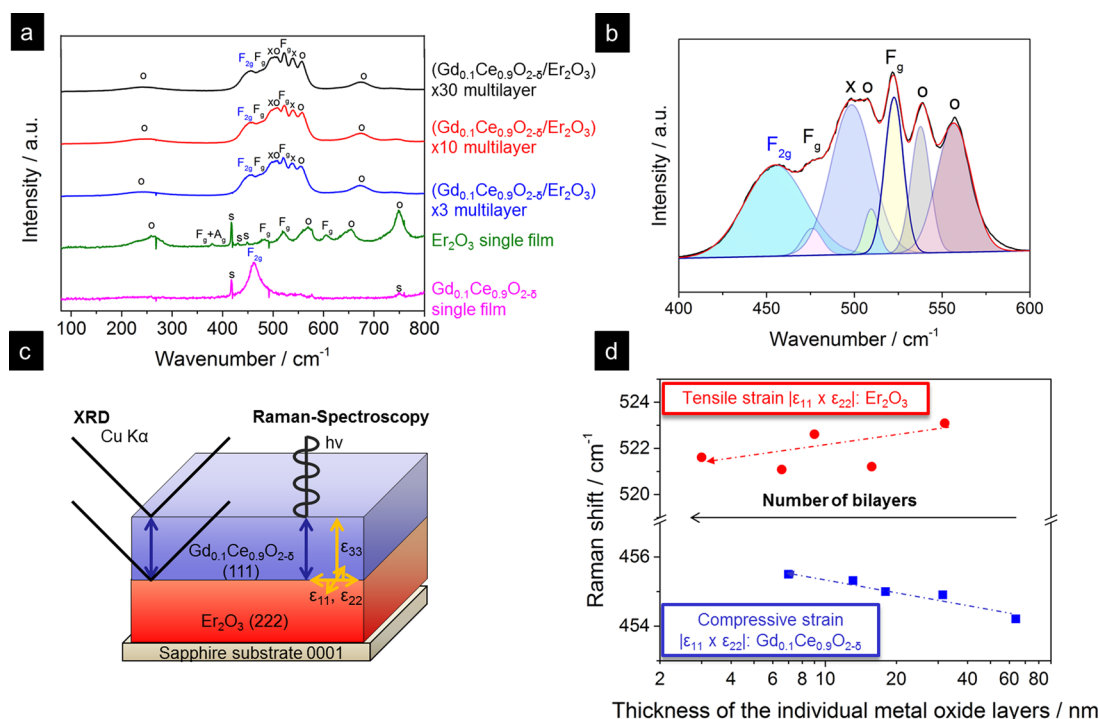
Figure 3. Near order Raman analysis of the Er_2O_3 and $Gd_{0.1}Ce_{0.9}O_{2-\delta}$ single thin films and multilayer thin films. (a) Raman spectra of the $Gd_{0.1}Ce_{0.9}O_{2-\delta}$ and Er_2O_3 single and multilayer thin films. The blue index indicates the F_{2g} mode of $Gd_{0.1}Ce_{0.9}O_{2-\delta}$ and the black F_g labels Er_2O_3. The (x) indicates unknown peaks, (o) identified ones matching with similar bixbyite structures. The peak assignments of the multilayer samples are tentative assignments. (b) Example of a Gaussian fit for the Raman spectra of a $(Gd_{0.1}Ce_{0.9}O_{2-\delta}/Er_2O_3) \times 10$ multilayer sample (tentative assignments). (c) Schematic view of the XRD and Raman measurement directions relative to the strained multilayer interface. The individual contributions of strain are shown by orange arrows. (d) Relative Raman wavenumber shift within multilayer film samples with respect to the individual metal oxide single layer thickness within Er_2O_3 and $Gd_{0.1}Ce_{0.9}O_{2-\delta}$ multilayers. The line of Er_2O_3 at ~520 cm^{-1} is shown in red, the line at ~455 cm^{-1} of $Gd_{0.1}Ce_{0.9}O_{2-\delta}$ is shown in blue. These peaks were used for data analysis. The in-plane strain is tensile for Er_2O_3 and compressive for $Gd_{0.1}Ce_{0.9}O_{2-\delta}$. The change of near order is measurable with increasing number of multilayers and strain at the interface. Total film thickness was kept constant at 275 nm.

TABLE 1. Assignment of the Observed Raman Peaks[a]

peak (app)/cm^{-1}	GDC pellet	Er_2O_3 pellet	GDC single film	Er_2O_3 single film	assignment	ref
230		x		x	match w. Sc_2O_3	66
250		x		x	match w. Sm_2O_3	66
380		x		x	$F_g + A_g$	60
465	x		x		F_{2g} of GDC	65
480		x		x	F_g of Er_2O_3	60
520		x		x	F_g of Dy_2O_3	60
560		x		x	match w. Mn_2O_3	66
600		x		x	F_g of Er_2O_3	60
660		x		x	match w. Mn_2O_3	66
750		x		x	match w. Sm_2O_3	66

[a] The peak positions are indicated in the first column and the peaks are assigned to Raman modes, if possible. Otherwise the peaks are matched with Raman spectra of rare earth oxides that crystallize in bixbyite structure.

chosen for analysis were the F_{2g} line (tentative assignment) of $Gd_{0.1}Ce_{0.9}O_{2-\delta}$ at ~455 cm^{-1} and the F_g line at ~520 cm^{-1} for Er_2O_3. The following observations can be made:

Increasing the number of interfaces and decreasing the single layer thickness of the multilayers results in

Raman peak shifts within the compressively strained ceria and tensely strained erbia $|\varepsilon_{11} \times \varepsilon_{22}|$ planes: For an increasing number of interfaces the F_{2g} Raman mode of ceria blue-shifts by 1.3 cm^{-1} (for increase from 5 to 59 interfaces). At the same time, the Raman erbia F_g mode red-shifts by 1.5 cm^{-1}. Using this strain-induced shift one can use the data provided by high-pressure studies[68] to estimate the strain in the heterostructure,[67] although we would like to note that strain in thin films cannot be directly compared to hydrostatic pressure. Regarding the elastic modulus used for the calculations one can use the bulk values for Gd-doped ceria,[69,70] resulting in change of the strain value of ~0.1%. But Kossoy[71] reported that the elastic modulus of thin films is more than 1 order of magnitude smaller than the value observed in bulk samples, resulting in change of the strain value of ~1.16% within the multilayer samples. For future discussions we will refer to the value estimated with the thin film elastic modulus.

We interpret this finding as lattice strain originating from the interfaces and relaxing over the thickness of each single layer. Therefore, thinner individual layers lead to increased strain at the heterointerfaces. This occurs for increased volume fractions of strained single layers when increasing the interface numbers within

the multilayered samples. This is in agreement with the data obtained by XRD.

Such behavior was predicted for the Yttria-stabilized zirconia system in density functional theory (DFT) and nudged elastic band (NEB) computational studies.[14] Earlier experimental studies reported the cationic order (measured by XRD) to be inconsistent on the single layer thickness or number of interfaces within the experimental error,[2] whereas in the present case the trends are consistent within the $Gd_{0.1}Ce_{0.9}O_{2-\delta}$/$Er_2O_3$ multilayer samples. Obtaining absolute values of the strain-induced Raman line shifts by comparing the Raman spectra of the multilayer samples with the samples of the single films was not possible due to the restrictions mentioned above.

Using this knowledge and data obtained by a high-pressure Raman study and general Raman theory a strain shift increasing the compressive in-plane strain in the $Gd_{0.1}Ce_{0.9}O_{2-\delta}$ and an increasing tensile in-plane shift for Er_2O_3 can be deduced.

In the given multilayer systems a decrease of single layer thickness of the $Gd_{0.1}Ce_{0.9}O_{2-\delta}$ phase increases the overall strained volume and the magnitude of strain as reported in the structural near order investigations, Figure 3. Through the following we study how the lattice strain affects the activation energy of conductivity for the multilayer microdots.

Impact of Lattice Strain on Electric Transport Characteristics of $Gd_{0.1}Ce_{0.9}O_{2-\delta}$/$Er_2O_3$ Multilayer for Sideways Contacted Microdot Device. The temperature dependence of conductivity was analyzed in Arrhenius plots for sideways contacted single and multilayer dots with respect to the strain activated volumes of the conductor, as shown in Figure 4a. The $Gd_{0.1}Ce_{0.9}O_{2-\delta}$ single film shows the highest conductivity with an activation energy of 0.75 eV in accordance with refs 18, 19, and 72. Increasing the number of $Gd_{0.1}Ce_{0.9}O_{2-\delta}$/$Er_2O_3$ interfaces and reducing the single layer thickness (down to 7 nm) for the small band gap $Gd_{0.1}Ce_{0.9}O_{2-\delta}$ results in an increase of ionic activation energy. The activation energy of conductivity is increased from 0.75 eV for the single film to 1.06 eV for the 59 interfaces sample, a change of activation energy $\Delta E_a = \Delta 0.31$ eV for $\sim$1.16% compressive strain imposed by the erbia phase of the multilayer on the $Gd_{0.1}Ce_{0.9}O_{2-\delta}$, Figure 4b,c. This trend is consistent throughout all multilayer samples. We attribute the increase in activation energy of ionic migration for the imposed compressive strain of erbia to the increased pressure acting on the strain activated volumes on the $Gd_{0.1}Ce_{0.9}O_{2-\delta}$ in consistency with eq 8–10. This corresponds to a change in enthalpy of oxygen migration of 0.31 eV for the strained $Gd_{0.1}Ce_{0.9}O_{2-\delta}$ phases of the multilayer according to the model expressed in eq 10. Further, the inset of Figure 4b shows the contacting strategy necessary to obtain measured data along the strained $| \varepsilon_{11} \times \varepsilon_{22} | Gd_{0.1}Ce_{0.9}O_{2-\delta}$ layers. Figure 4c displays the decrease of ionic conductivity

while minimizing the thickness of the individual $Gd_{0.1}Ce_{0.9}O_{2-\delta}$ single layers and maximizing the strain volume for the ceria-phase. It can be concluded that a clear impact of the compressively strained volumes of the small band gap conductor on its ionic transport is reported for sideways contacted microdot structures. Accordingly, we summarize in Figure 4d that all strained ceria-based single layers contribute to the overall transport of the microdot structures through the pathways P1 + P3 outlined in the circuit model. The insulating wide band gap erbia single layers of the dot do not contribute with the pathways P2 + P4, but act as strain modulators of the ceria-phase for the microdot.

Defect Thermodynamic Model for Strain-Modulated $Gd_{0.1}Ce_{0.9}O_{2-\delta}$/$Er_2O_3$ Multilayer Microdot Device Structures. In the following, we discuss the concept of sideways contacted $Gd_{0.1}Ce_{0.9}O_{2-\delta}$ and Er_2O_3 multilayer microdots in their ionic transport characteristics for modified interfacial strains. For a multilayer microdot, the gadolinia-doped ceria single layers represent the small band gap phase with a band gap of 3.1 eV[73] and a predominantly oxygen ionic conductivity with an activation energy of ionic conductivity of $\sim$0.75 eV in air for bulk.[72] On the other hand the erbia single layers of the multilayer dots are the wide band gap phase with a band gap of 7.6 eV[74] and an ionic activation energy of $\sim$1.6 eV in air for bulk.[75] On the basis of bulk transport data, it is to be expected that the erbia single layer phases block the electric field lines for sideways contacting in the multilayer. The current is carried by the ionic conducting $Gd_{0.1}Ce_{0.9}O_{2-\delta}$ single layers of the multilayer microdot for sideways electrode arrangements measuring along the strained interfaces. The erbia's sole function in the multilayer is to modify the interatomic distances locally at the interface by imposing a compressive strain on the ionic current carrying $Gd_{0.1}Ce_{0.9}O_{2-\delta}$ phase. We keep the film thickness in all experiments constant and vary systematically the number of interfaces and single layer thicknesses of $Gd_{0.1}Ce_{0.9}O_{2-\delta}$ and Er_2O_3 phases in the multilayers. Consequently, we consider that due to big differences in the conductivity of the two materials, either the $Gd_{0.1}Ce_{0.9}O_{2-\delta}$ or the interfaces are relevant for the conduction, while the bulk Er_2O_3 phase is an electrical insulator and only serves as matrix to achieve the desired strain state variation in the $Gd_{0.1}Ce_{0.9}O_{2-\delta}$ (GDC) phase by the lattice misfit of the two adjacent materials: The lattice misfit f between the two materials, erbia and gadolinia-doped ceria with the lattice constants $a_{Er_2O_3}$ and a_{GDC}, in the following denoted as a_ε (since the $Gd_{0.1}Ce_{0.9}O_{2-\delta}$ phase is the conducting phase under strain) with respect to erbia is defined as

$$f = \frac{a_{Er_2O_3} - a_\varepsilon}{a_{Er_2O_3}} \quad (2)$$

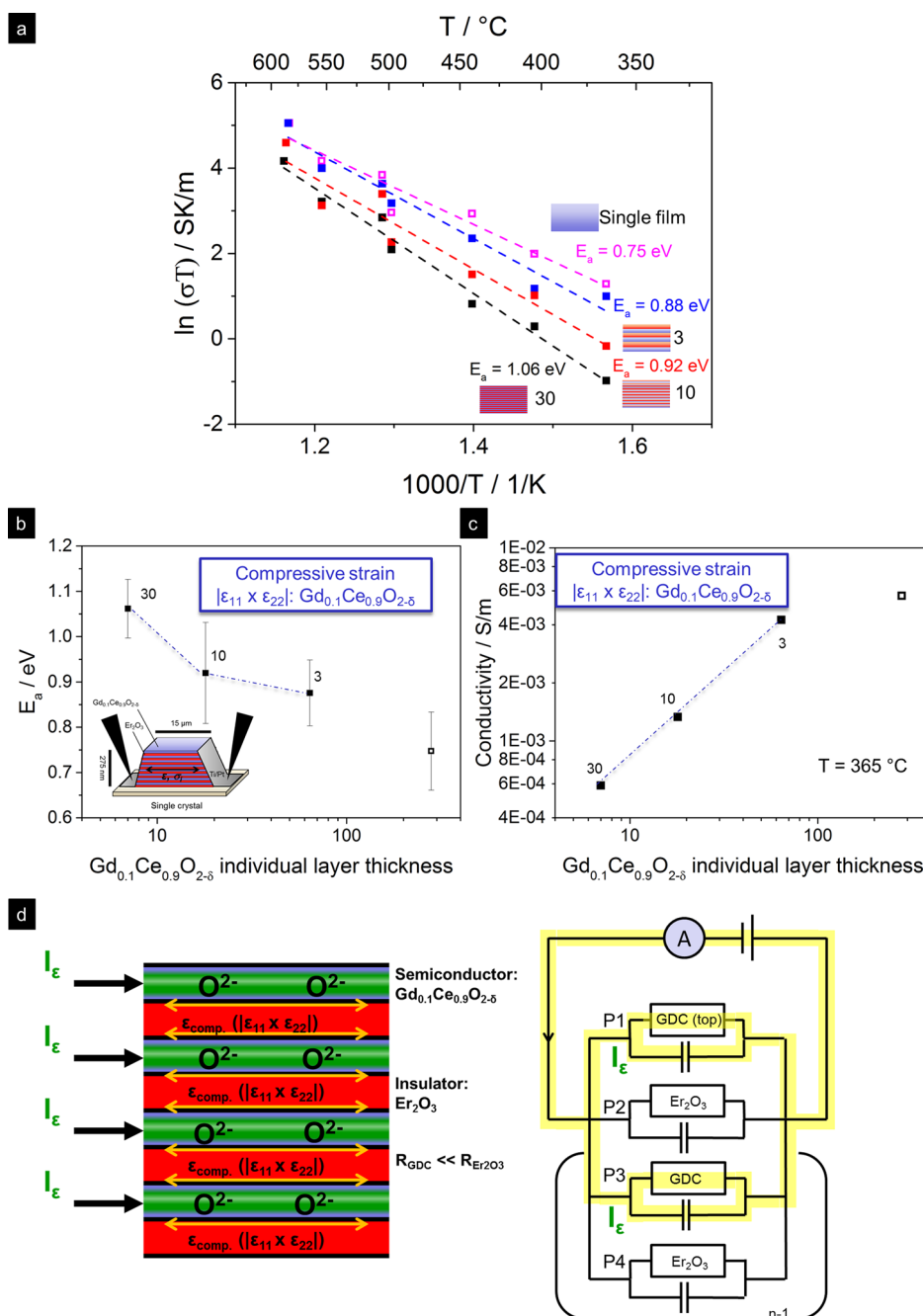and gives a numerical value of the theoretical lattice misfit of 2.74%, acting compressively on the

Figure 4. Ionic conductivity for the sideways contacted and strain modulated $Gd_{0.1}Ce_{0.9}O_{2-\delta}/Er_2O_3$ multilayer micro-dots. (a) Arrhenius plot of the conductivity for $Gd_{0.1}Ce_{0.9}O_{2-\delta}$ single thin film *vs* $Gd_{0.1}Ce_{0.9}O_{2-\delta}/Er_2O_3$ multilayer thin film microdots for sideways contacting. The numbers next to the specimens indicate the number of bilayers. (b) Activation energy with respect to the thickness of the individual single layer thickness of $Gd_{0.1}Ce_{0.9}O_{2-\delta}$. The measurement setup is shown in the inset. The total change of activation energy is $\triangle 0.31$ eV. The inset shows the measurement setup that allows measurement of the whole multilayer structure. The open symbol refers to the single film. (c) Plot of electric conductivities of the $Gd_{0.1}Ce_{0.9}O_{2-\delta}$ single thin film and $Gd_{0.1}Ce_{0.9}O_{2-\delta}/Er_2O_3$ multilayer thin films with respect to the thickness of $Gd_{0.1}Ce_{0.9}O_{2-\delta}$ for 365 °C. The open symbol refers to the single film. (d) Schematic view graphic on conduction pathways and electronic circuit model for the $Gd_{0.1}Ce_{0.9}O_{2-\delta}/Er_2O_3$ multilayer microdots. Left: Model of the current flow in the specimen for $R_{GDC} \ll R_{Er2O3}$. Here, the ionic current flows through all semiconducting layers of the $Gd_{0.1}Ce_{0.9}O_{2-\delta}$ phase. The Er_2O_3 phase does not contribute to the electric conductivity, but serves as phase to tune the compressive strain acting on the $Gd_{0.1}Ce_{0.9}O_{2-\delta}$ phase of the microdot structure. Right: Equivalent circuit model and ionic pathways of the microdot device. The yellow shading indicates the flow of the ionic current along P1 + P3 and strain modulation within the $Gd_{0.1}Ce_{0.9}O_{2-\delta}$ RC circuit elements of a microdot. Blocking for the strain modulating pathways P2 + P4 is indicated. Total thin film structure thickness was kept constant at 275 nm.

$Gd_{0.1}Ce_{0.9}O_{2-\delta}$ single layers. The ionic conduction of the latter small band gap phase is described by an oxygen ion hopping mechanism *via* oxygen vacancies,[76] which are the predominant charge carrier introduced through

doping, as shown in eq 3.

$$Gd_2O_3 \xrightarrow{CeO_2} 2Gd_{Ce}' + 3O_O^x + V_O^{\bullet\bullet} \quad (3)$$
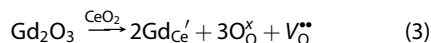
The wide-band gap phase erbia reveals p-type conduction as predominant mechanism in air.[75] The predominant fast ceria-based ionic conductivity, σ_{ionic}, of the multilayer microdot for measurement along the interfaces is given by

$$\sigma_{ionic}(T) = (2q)[V_O^{\bullet\bullet}]v_i$$
$$= (2q)[V_O^{\bullet\bullet}]\frac{v_{0i}}{T}\exp\left(-\frac{\Delta H_{mig}}{k_B T}\right) \quad (4)$$

$2q$ represents the charge of an oxygen vacancy, $[V_O^{\bullet\bullet}]$ refers to the oxygen vacancy concentration, v_i stands for the ionic mobility, v_{0i} is the pre-exponential ionic mobility factor, ΔH_{mig} is the enthalpy of oxygen vacancy migration, and k_B is Boltzmann's constant. For the sake of completeness it has to be mentioned that the overall measured ionic activation energy E_a of the strained volumes consists of the enthalpy of oxygen vacancy migration ΔH_{mig} and the enthalpy of oxygen vacancy-dopant associate formation ΔH_{assoc} through

$$\Delta E_a = \Delta H_{mig} + \Delta H_{assoc} \quad (5)$$

We consider predominantly the migration enthalpy to change, and refer for discussion of defect associations to refs 77−82. Therefore, in the following the activation energy is treated to be represented in good approximation by the migration enthalpy. The total volume change is negligibly small for solids; therefore, energy and enthalpy are considered to be equal.

One can express eq 4 in terms of the oxygen ionic diffusion coefficient, D_{ionic}, being proportional to the square of the jump distance d and its oxygen ionic hopping frequency ω by

$$\sigma_{ionic}(T) = \frac{(2q)^2[V_O^{\bullet\bullet}]}{k_B T}D_{ionic} = \frac{(2q)^2[V_O^{\bullet\bullet}]}{k_B T}d^2\omega \quad (6)$$

$$= \frac{(2q)^2[V_O^{\bullet\bullet}]^2}{k_B T}a_\varepsilon{}^2\omega\alpha_\varepsilon \quad (7)$$

The jump distance d is directly related to the lattice constant a_ε of the $Gd_{0.1}Ce_{0.9}O_{2-\delta}$ and strain state due to its cubic fcc lattice structure nature, eq 6. For oxygen ionic hopping over vacancies in the strained fcc lattice the geometry factor $\alpha_\varepsilon = 1$. It is important to note that modifications of the strain tensor elements may lower symmetry and, hence, affect in eq 6 both the geometry factor and strained lattice constant a_ε for the conducting $Gd_{0.1}Ce_{0.9}O_{2-\delta}$. This could also potentially alter Poisson's ratio.

We can assume the only quantity that is significantly influenced by strain is the migration enthalpy ΔH_{mig}, all other quantities are hardly affected by

TABLE 2. Calculated Strain Activation Volumes for the Multilayer Thin Film System Investigated

specimen	strain activation volume/cm³ mol⁻¹
$(Gd_{0.1}Ce_{0.9}O_{2-\delta}/Er_2O_3) \times 3$	3.03
$(Gd_{0.1}Ce_{0.9}O_{2-\delta}/Er_2O_3) \times 10$	3.96
$(Gd_{0.1}Ce_{0.9}O_{2-\delta}/Er_2O_3) \times 30$	7.22

strain.[2,83,84] Thermodynamically the $Gd_{0.1}Ce_{0.9}O_{2-\delta}$ strain activated volume, ΔV_{mig}, of ionic migration (and possible contributions of association, included in the migration enthalpy) depends on the applied hydrostatic pressure p imposed by the erbia single layers in the multilayer dot; this is in accordance to De Souza's models[83,84] and is described in good approximation by the following equation:

$$\Delta V_{mig, eff} = \frac{\partial \Delta G_{mig}}{\partial p_{eff}} \quad (8)$$

where ΔG_{mig} stands for the Gibb's energy of migration. The Gibb's free energy is given by

$$\Delta G_{mig} = \Delta E_{mig} - T\Delta S_{mig} - \sigma\Delta V_{mig} \quad (9)$$

for a system influenced by the strain tensor σ. Neglecting the activation entropy and considering the case of biaxial strain, we can rewrite eq 8 using eq 9 to

$$\Delta H_{mig} = \Delta E_{mig} - \frac{2}{3}\sigma_{xx}\Delta V_{mig} \quad (10)$$

The biaxial strain σ_{xx} is then given by

$$\sigma_{xx} = 3B\frac{1-2v}{1-v}\frac{a-a_\varepsilon}{a_\varepsilon} \quad (11)$$

B denotes the bulk modulus, v Poisson's ratio, and a and a_ε the lattice constants of the unstrained and strained material, respectively. Using the lattice mismatch and above presented equations the activation volumes of the strained multilayer thin film samples could be calculated; see Table 2. The resulting strain activated volumes range from 3.03 to 7.22 cm³ mol⁻¹ and correspond to a change in ionic activation energy of 0.75 to 1.06 eV for an increase of 6 to 60 single layers in the multilayer, i.e. $(Gd_{0.1}Ce_{0.9}O_{2-\delta}/Er_2O_3) \times 3$ to $(Gd_{0.1}Ce_{0.9}O_{2-\delta}/Er_2O_3) \times 30$. Using the consideration of elastic moduli in bulk and thin film samples presented above this corresponds to a change of strain of 0.1 or 1.16%, estimated from Raman spectroscopy. For the constants used in the calculations; see refs 69−71. The change in activation volume is increased for highly strained structures. De Souza states that the activation volume of fluorite-structured oxides is 1 to 2 cm³ mol⁻¹ for pressures below 1 GPa.[83]

Role of Microelectrode Contacting and Geometry in Measuring Strain-Ionic Transport Modulations for Microelectrochemical Devices. State-of-the-art electrical contacting operates either *via* placing of top in-plane electrode contacts on a strained multilayer film or by macroscopically
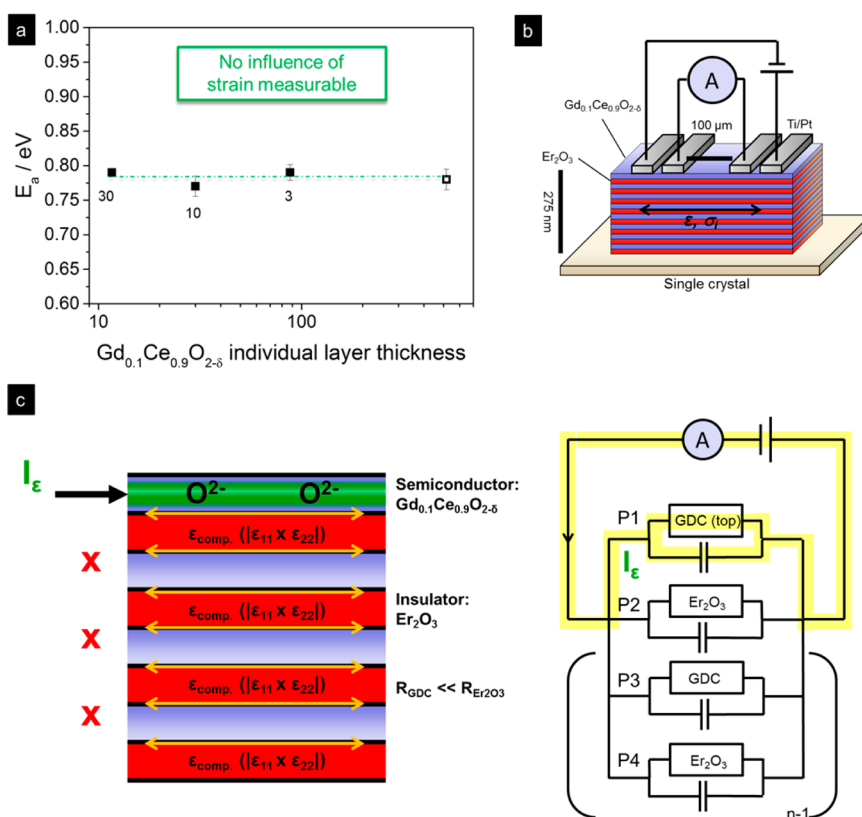
a

No influence of strain measurable

E_a / eV

30 10 3

$Gd_{0.1}Ce_{0.9}O_{2-\delta}$ individual layer thickness

b

A

$Gd_{0.1}Ce_{0.9}O_{2-\delta}$ 100 μm Ti/Pt

Er_2O_3

275 nm

ε, σ_i

Single crystal

c

I_ε

O^{2-} O^{2-} Semiconductor: $Gd_{0.1}Ce_{0.9}O_{2-\delta}$

$\varepsilon_{comp.}$ ($|\varepsilon_{11} \times \varepsilon_{22}|$)

X $\varepsilon_{comp.}$ ($|\varepsilon_{11} \times \varepsilon_{22}|$) Insulator: Er_2O_3

X $\varepsilon_{comp.}$ ($|\varepsilon_{11} \times \varepsilon_{22}|$) $R_{GDC} \ll R_{Er2O3}$

X $\varepsilon_{comp.}$ ($|\varepsilon_{11} \times \varepsilon_{22}|$)

A

P1 GDC (top)

I_ε

P2 Er_2O_3

P3 GDC

P4 Er_2O_3

n-1

Figure 5. Ionic conductivity for top-electrode contacted and strain modulated $Gd_{0.1}Ce_{0.9}O_{2-\delta}$/$Er_2O_3$ multilayer films. (a) Arrhenius plot of the conductivity for $Gd_{0.1}Ce_{0.9}O_{2-\delta}$ single thin film vs $Gd_{0.1}Ce_{0.9}O_{2-\delta}$/$Er_2O_3$ multilayer thin films for classic top in-plane electrode contacting. The numbers next to the specimens indicate the number of bilayers. (b) The measurement setup is shown for top in-plane electrode contacting. The activation energy remains invariant on the strain state of the multilayer. The classic measurement setup is not suited to measure real strain effects on ionic transport. (c) Schematic view graphic on conduction pathways and electronic circuit model for the classically contacted $Gd_{0.1}Ce_{0.9}O_{2-\delta}$/$Er_2O_3$ multilayer. Left: Model of the current flow in the specimen for $R_{GDC} \ll R_{Er2O3}$. Here, the ionic current flows only through the topmost $Gd_{0.1}Ce_{0.9}O_{2-\delta}$ layer; it gets blocked at the subsequent insulating erbia layer, and other strained $Gd_{0.1}Ce_{0.9}O_{2-\delta}$ films do not contribute to the current in the device. Right: Equivalent circuit model and ionic pathways of the classically contacted multilayer film. The yellow shading indicates the flow of the ionic current going only along P1 (topmost layer). All other pathways P2−P4 do not contribute to the electronic circuit.

painting metal electrodes at the sides of the multilayer structure.[5,85] As discussed in the introduction both strategies may not be applicable for implementation of strained multilayer oxides as functional building blocks for new microelectrochemical chip devices. Nevertheless, we exemplify the state-of-the-art contacting of similarly strained $Gd_{0.1}Ce_{0.9}O_{2-\delta}$/$Er_2O_3$ multilayers via deposition of top in-plane electrodes; see Figure 5a,b. Although the thickness of the individual single layers was changed over a wide range to affect the strain activated volumes of the small band gap $Gd_{0.1}Ce_{0.9}O_{2-\delta}$ phase no change of activation energy was measurable. Similar observations were made for the effective ionic conductivity measured as invariant on strain activated volume of the ceria single layers for the contacted top-electrodes. Using state-of-the-art top-electrode contacting it can be assumed that only the topmost layer is contributing to the total conductivity via pathway P1 of the equivalent circuit model in Figure 5c. Here, the pathways P2−P4 of the circuit model (i.e., the strained volume fractions) do not

contribute to the overall conductivity measured through the top-electrode approach. The electric field lines get restricted and blocked off at the subsequent insulating erbia single layer. Hence, no strain effect is measurable even though it is present in the sample for state-of-the-art top-electrode contacting of the multilayer. This clearly demonstrates the need for sideways contacting and alternative strategies for microdot based devices with sideways contacting.

Literature reports on multilayers for which despite the structural proof no effect of strain on ionic transport of the structures was measurable, i.e., for top in-plane electrode contacted YSZ/CeO_2 multilayers or strained Gd-doped ceria films.[25−27] For that case alteration of the microelectrode design relative to the strain tensor elements and activated volumes of the conductive multilayer component is of importance.

CONCLUSION

We demonstrate a new strategy to fabricate ionic conducting gadolinia-doped ceria/erbia multilayer

dot array structures, illustrate the feasibility of sideways dot contacting for 2 orders of magnitude smaller distances (15 μm) toward the state-of-the-art, and show that the ionic conductivity activation energy of the small conducting ceria-based phase can be manipulated by the compressively imposed strain activated volumes through the erbia for a multilayer dot.

All multilayer thin film dots show the orientation aimed for; *i.e.*, successful biaxial texturing of the metal oxide thin films on the sapphire substrates can be concluded. To get insight into the interfacial state, Raman spectroscopy was applied to investigate the cation–anion-near order. Changes in the strain state can be correlated to a relative change of the positions of the Raman shifts and the sensitivity of this method allows observing increasing strain at the interface as the proportion of strained volume is increased. Regarding the activation energy, a change of $\Delta 0.31$ eV can be observed for ~1.16% relative strain for the ceria-based phase in the multilayer samples.

Our findings have the following implications for the future design of microelectrochemical devices based on strain oxide modulation.

First, a strategy to fabricate such electrochemical heterostructures as microdevices is presented. This strategy allows exploiting the altered flux of charge carriers along the interfaces parallel to the surface for a sideways controlled ionic conducting multilayer dot. For example, our work opens the possibility to replace classic single metal oxide films in future resistive switches by a functional strained multilayer dot. The broad range for which we can alter the ionic conductivity activation energy through compressive strain, in the given example of ceria single layers for the multilayer dot, would not be achievable by classic doping or changes of nonstoichiometry for a resistive switch functional oxide film. Hence, we can use the interfacial strain of such multilayer dots and short electrode distances to actively tune the desired resistive properties in their memristive and memcapacitive properties in follow-up studies. The short electrode distances were a prerequisite to reach typical local electric field strengths of about $>10^6$ V/m.[36] The presented fabrication strategy together with the concept of microdots with strained internal interfaces is a promising avenue for novel electrochemical microdevices, *e.g.*, energy conversion and storage devices, information technology devices, or sensors.

Second, we contribute with a hands-on proof-of-concept to the ongoing debate on the role of microelectrode contacting for strained ionic conducting multilayers. Revealing that the classical top in-plane electrode approach is not suitable to measure real strain effects for the given case of erbia/gadolinia-doped ceria multilayers, the change in activation energy is nil for a broad range of number of interfaces varied (ranging from a single layer thickness from 300 to 6) even though there is structural proof for strain. Measuring the same multilayer structures with the sideways contacted microdot approach reveals that a *real strain effect* is indeed measured. Defect thermodynamics and strain activated volume model were well applied to describe the change of conductivity and activation energy for the multilayers.

Third, to date it was challenging to compare strain-ionic transport results obtained by different research groups for multilayer systems based on zirconia or ceria single layers as a conductive phase. Looking forward, the quantitative analysis of near order and ionic bond strength of the anionic-cationic lattice that can be measured by Raman punctuates its potential with respect to a multilayer's film growth, processing, and chemistry. State-of-the-art literature considers cationic disorder to be characterized by XRD, and so very often no clear trends were observable relative to the varying strain activated volumes. However, we report that there are observable near order relaxation processes relative to the strain activated volume occurring on the near order and confirm earlier computational study predictions.

METHODS

Material Synthesis. $Gd_{0.1}Ce_{0.9}O_{2-\delta}$ and Er_2O_3 single thin films and multilayer thin films composed of the two oxide materials were synthesized in this study.

The thin films were deposited on round single crystalline, double-side polished (0001)-oriented sapphire substrates (Stettler sapphire, Switzerland) by pulsed laser deposition (PLD, Surface Technologies, Germany; KrF excimer laser, 248 nm). The thin films were deposited at 60 mJ per pulse at a repetition rate of 10 Hz for a substrate to target distance of 8.5 cm. After reaching a background pressure of 4×10^{-6} mbar, the films were deposited at 700 °C and 0.0267 mbar O_2 pressure. In this study a constant film thickness of 275 nm was aimed for all samples (single films and multilayers). This corresponds to 14 000 pulses for the $Gd_{0.1}Ce_{0.9}O_{2-\delta}$ single film sample, 21 000 pulses for the multilayer heterostructure samples, and 26 000 pulses for the Er_2O_3 single film sample.

Subsequent profilometer measurements Dektak XT Advanced profilometer (Bruker, Germany) and SEM cross-sectional analysis were used to verify the constant film thickness within an error of 10% throughout this study. For the multilayer PLD depositions repetitions of $Gd_{0.1}Ce_{0.9}O_{2-\delta}$ and Er_2O_3 single layers were deposited on the sapphire substrates. The single layer thickness of either $Gd_{0.1}Ce_{0.9}O_{2-\delta}$ or Er_2O_3 was varied from 280 (255) to 7 (3) nm while the overall film thickness was kept at constant 275 nm. As a consequence, the number of $Gd_{0.1}Ce_{0.9}O_{2-\delta}/Er_2O_3$ interfaces varied from 5 to 59 within the films, corresponding to a number of single layers of 6 to 60 in the multilayer structures, also denoted as $(Gd_{0.1}Ce_{0.9}O_{2-\delta}/Er_2O_3) \times 3$ to $(Gd_{0.1}Ce_{0.9}O_{2-\delta}/Er_2O_3) \times 30$. Substrates were always cleaned in an ultrasound bath with acetone, isopropanol, and deionized water prior to film deposition.

Ceramic targets for the pulsed laser deposition, $Gd_{0.1}Ce_{0.9}O_{2-\delta}$ (Praxair, Woodinville, WA) and Er_2O_3 (Sigma-Aldrich, Switzerland)
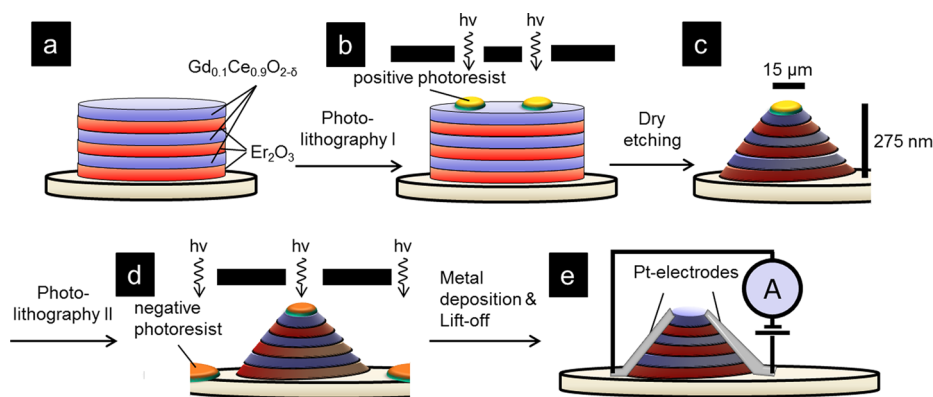
Figure 6. Schematic thin film and microfabrication process flow for $Gd_{0.1}Ce_{0.9}O_{2-\delta}$/$Er_2O_3$ multilayer microdots. (a) Laser ablated multilayer thin film on an oriented sapphire substrate. (b) A pattern of photoresist dots was structured on the surface (first positive photolithography step). (c) Ar^+ sputtering was applied to 3D-shape the multilayer thin films. (d) Photoresist pattern for electrodes are shaped (second negative photolithography step) (e) Pt metal contacts deposition on the side walls of the single and multilayer thin films. The dimensions are not to scale.

were processed from powders. The targets were uniaxially and then isostatically pressed (440 bar for 2 min) from powder, heated to 1650 °C (Er_2O_3)/1400 °C ($Gd_{0.1}Ce_{0.9}O_{2-\delta}$) at 5 °C/min, isothermally held for 24 h (Er_2O_3)/4 h ($Gd_{0.1}Ce_{0.9}O_{2-\delta}$) and then cooled at 5 °C/min to room temperature. The target phases were characterized by X-ray Diffraction (Bruker D8, Cu Kα).

Microdevice and Electrode Preparation: Lithography and Microfabrication. In this experimental part sideways attached electrodes were designed and microprocessed to measure conduction properties along the strained multilayer interfaces for small electrode distances of 15 μm; see Figure 6. Two challenges had to be considered in the planning: First, multilayers with variable number of interfaces had to be etched under an angle of roughly 80° toward the substrate to subsequently deposit metal electrodes that contact all single layers and strained interfaces over the sides of the microdevice. Next, a second lithography step was required to allow for electrode depositions at 15 μm distance and an overlap of roughly 2 μm between the top of the multilayer film and its side flank. It is to be noted that we report a new micropatterning route for the fabrication of sideways electric contacting of strained multilayer oxides with small scale microelectrodes.

In the following we detail the experimental fabrication steps for the small-scale "side-plane" microelectrodes; see schematic in Figure 6. All steps were carried in an ISO class 4 cleanroom. Multilayer thin films on sapphire samples (Figure 6a) were subjected in a first step to the shaping of the side flanks and top film area. For this, a foil mask (Selba, Switzerland) and AZ 1518 positive photoresist (Microchemicals, Germany) were used in a first photolithography step: the photoresist was spin-coated onto the sample surface at a rotation speed of 4000 rpm for 30 s and baked at 100 °C for 120 s. The samples were then aligned (Karl-Suss MJB3 mask aligner) and exposed through a foil lithography mask to broadband ultraviolet light with a dose of 74 mJ/cm^2 (Figure 6b). The pattern was developed using MIF 726 developer (Microchemicals, Germany). After the first pattern of regularly distributed photoresist islands was made on the samples the ceramic thin film was dry-etched using argon ion (Ar^+) sputtering (Oxford Instruments Plasmalab 80) (Figure 6c). Subsequently, the remaining photoresists was removed using acetone. In order to get well-defined electrodes a second photolithography step similar to the first one was done using AZ nLOF 2070 (1:0.4) negative photoresist (Microchemicals, Germany) The samples were spinned at a speed of 4750 rpm for 45 s and then softbaked at 110 °C for 90 s. The second photoresist pattern was aligned over the ceramic microdots by visual alignment overlapping 2 μm with the help of alignment marks. Then they were exposed to a light dose of 210 mJ/cm^2, and subsequently the photoresists was subject to another heating step at 110 °C for 180 s (Figure 6d). Finally the pattern was developed using the MIF 726 developer.

In the last step metal electrodes constituting of Ti 25 nm/Pt 150 nm were deposited via electron beam evaporator (Plassys MEB 550, France). Ultimately, the samples were soaked in acetone until the remaining photoresist was stripped off, as determined by visual inspection. The height profile of the microdot island was investigated by optical surface profilometry (Sensofar Plu neox, Spain).

Chemical and Structural Characterization. The as-deposited single and multilayer films were characterized by X-ray Diffraction (Bruker D8) at a Cu Kα wavelength. Raman spectroscopy was performed using a confocal WITec CRM200 Raman microscope instrument (WITec, Germany) equipped with a 532 nm wavelength laser for excitation and a spectral resolution of 0.7 cm^{-1}. Fitting was done by OriginPro 9.1 using a Gaussian function. The error of the fit ranges from 0.14 to 0.017%. One fit is depicted exemplarily in Figure 3b. Materials were characterized with a scanning electron microscope (SEM, LEO 1530, Germany) to analyze the microstructures.

Electrical Characterization. DC 4-point electric conductivity measurements of the thin film microdevice structures were performed in air using the Keithley 2601B multimeter for kinetic measurements with applied DC voltage amplitude of 1 V. The thin film microdevice structures were contacted with tungsten microprobe tips in a custom fabricated microprobe station (Everbeing, Taiwan and Electrochemical Materials ETH Zurich, Switzerland) with a sealed air atmosphere environment, equipped with stereomicroscopy. The temperature was varied during the measurements between room temperature and 585 °C at heating/cooling rates of 5 °C/min. To get kinetic reference data measurements were done on bulk pellets contacted by Pt paste and wire in a tube furnace. The temperature range was from room temperature to 1000 °C with heating/cooling rates of 5 °C/min.

Conflict of Interest: The authors declare no competing financial interest.

Supporting Information Available: Section 1 provides spatially resolved Raman scans of the microdot array. Section 2 shows detailed XRD Scans of the thin film samples. Section 3 presents the XRD patterns of pellets used for sample preparation. Section 4 compares the Raman spectra of $Gd_{0.1}Ce_{0.9}O_{2-\delta}$

and Er_2O_3 of pellets and single thin film samples. This material is available free of charge *via* the Internet at http://pubs.acs.org.

REFERENCES AND NOTES

1. Azad, S.; Marina, O. A.; Wang, C. M.; Saraf, L.; Shutthanandan, V.; McCready, D. E.; El-Azab, A.; Jaffe, J. E.; Engelhard, M. H.; Peden, C. H. F.; *et al.* Nanoscale Effects on Ion Conductance of Layer-by-Layer Structures of Gadolinia-Doped Ceria and Zirconia. *Appl. Phys. Lett.* **2005**, *86*, 131906.

2. Korte, C.; Peters, A.; Janek, J.; Hesse, D.; Zakharov, N. Ionic Conductivity and Activation Energy for Oxygen Ion Transport in Superlattices—the Semicoherent Multilayer System YSZ ($ZrO_2+9.5$ mol% Y_2O_3)/Y_2O_3. *Phys. Chem. Chem. Phys.* **2008**, *10*, 4623–4635.

3. Korte, C.; Schichtel, N.; Hesse, D.; Janek, J. Influence of Interface Structure on Mass Transport in Phase Boundaries Between Different Ionic Materials Experimental Studies and Formal Considerations. *Monatsh. Chem.* **2009**, *140*, 1069–1080.

4. Schichtel, N.; Korte, C.; Hesse, D.; Janek, J. Elastic Strain at Interfaces and its Influence on Ionic Conductivity in Nanoscaled Solid Electrolyte Thin Films—Theoretical Considerations and Experimental Studies. *Phys. Chem. Chem. Phys.* **2009**, *11*, 3043–3048.

5. Peters, A.; Korte, C.; Hesse, D.; Zakharov, N.; Janek, J. Ionic Conductivity and Activation Energy for Oxygen Ion Transport in Superlattices—The Multilayer System CSZ (ZrO_2+CaO)/Al_2O_3. *Solid State Ionics* **2007**, *178*, 67–76.

6. Garcia-Barriocanal, J.; Rivera-Calzada, A.; Varela, M.; Sefrioui, Z.; Iborra, E.; Leon, C.; Pennycook, S. J.; Santamaria, J. Colossal Ionic Conductivity at Interfaces of Epitaxial ZrO_2: Y_2O_3/$SrTiO_3$ Heterostructures. *Science* **2008**, *321*, 676–680.

7. Hirschfeld, J. A.; Lustfeld, H. First-Principles Study and Modeling of Strain-Dependent Ionic Migration in ZrO_2. *Phys. Rev. B: Condens. Matter Mater. Phys.* **2011**, *84*, 224308.

8. Dezanneau, G.; Hermet, J.; Dupe, B. Effects of Biaxial Strain on Bulk 8% Yttria-Stabilised Zirconia Ion Conduction Through Molecular Dynamics. *Int. J. Hydrogen Energy* **2012**, *37*, 8081–8086.

9. Lee, K. R.; Ahn, K.; Chung, Y. C.; Lee, J. H.; Yoo, H. I. Lattice Distortion Effect on Electrical Properties of GDC Thin Films: Experimental Evidence and Computational Simulation. *Solid State Ionics* **2012**, *229*, 45–53.

10. Sata, N.; Eberman, K.; Eberl, K.; Maier, J. Mesoscopic Fast Ion Conduction in Nanometre-Scale Planar Heterostructures. *Nature* **2000**, *408*, 946–949.

11. Sanna, S.; Esposito, V.; Tebano, A.; Licoccia, S.; Traversa, E.; Balestrino, G. Enhancement of Ionic Conductivity in Sm-Doped Ceria/Yttria-Stabilized Zirconia Heteroepitaxial Structures. *Small* **2010**, *6*, 1863–1867.

12. Guo, X. Comment on "Colossal Ionic Conductivity at Interfaces of Epitaxial ZrO_2:Y_2O_3/$SrTiO_3$ Heterostructures". *Science* **2009**, *324*, 465.

13. Kilner, J. A. Ionic Conductors Feel the Strain. *Nat. Mater.* **2008**, *7*, 838–839.

14. Kushima, A.; Yildiz, B. Oxygen Ion Diffusivity in Strained Yttria Stabilized Zirconia: Where is the Fastest Strain? *J. Mater. Chem.* **2010**, *20*, 4809–4819.

15. De Souza, R. A.; Ramadan, A. H. H. Ionic Conduction in the $SrTiO_3$ | YSZ | $SrTiO_3$ Heterostructure. *Phys. Chem. Chem. Phys.* **2013**, *15*, 4505–4509.

16. Aydin, H.; Korte, C.; Rohnke, M.; Janek, J. Oxygen Tracer Diffusion Along Interfaces of Strained Y_2O_3/YSZ Multilayers. *Phys. Chem. Chem. Phys.* **2013**, *15*, 1944–1955.

17. Schichtel, N.; Korte, C.; Hesse, D.; Zakharov, N.; Butz, B.; Gerthsen, D.; Janek, J. On the Influence of Strain on Ion Transport: Microstructure and Ionic Conductivity of Nanoscale YSZ | Sc_2O_3 Multilayers. *Phys. Chem. Chem. Phys.* **2010**, *12*, 14596–14608.

18. Rupp, J. L. M. Ionic Diffusion as a Matter of Lattice-Strain for Electroceramic Thin Films. *Solid State Ionics* **2012**, *207*, 1–13.

19. Rupp, J. L. M.; Fabbri, E.; Marrocchelli, D.; Han, J.-W.; Chen, D.; Traversa, E.; Tuller, H. L.; Yildiz, B. Scalable Oxygen-Ion Transport Kinetics in Metal-Oxide Films: Impact of Thermally Induced Lattice Compaction in Acceptor Doped Ceria Films. *Adv. Funct. Mater.* **2014**, *24*, 1562–1574.

20. Omar, S.; Wachsman, E. D.; Nino, J. C. Higher Conductivity Sm^{3+} and Nd^{3+} Co-Doped Ceria-Based Electrolyte Materials. *Solid State Ionics* **2008**, *178*, 1890–1897.

21. Schweiger, S.; Messerschmitt, F.; Rupp, J. L. M. Patent Application EP13002075.3, Strained Multilayer Resistive-Switching Memory Elements, 2013.

22. Santiso, J.; Burriel, M. Deposition and Characterisation of Epitaxial Oxide Thin Films for SOFCs. *J. Solid State Electrochem.* **2011**, *15*, 985–1006.

23. Sillassen, M.; Eklund, P.; Pryds, N.; Johnson, E.; Helmersson, U.; Bottiger, J. Low-Temperature Superionic Conductivity in Strained Yttria-Stabilized Zirconia. *Adv. Funct. Mater.* **2010**, *20*, 2071–2076.

24. Kosacki, I.; Rouleau, C. M.; Becher, P. F.; Bentley, J.; Lowndes, D. H. Nanoscale Effects on the Ionic Conductivity in Highly Textured YSZ Thin Films. *Solid State Ionics* **2005**, *176*, 1319–1326.

25. Pergolesi, D.; Fabbri, E.; Cook, S. N.; Roddatis, V.; Traversa, E.; Kilner, J. A. Tensile Lattice Distortion Does Not Affect Oxygen Transport in Yttria-Stabilized Zirconia-CeO_2 Heterointerfaces. *ACS Nano* **2012**, *6*, 10524–10534.

26. Chen, L.; Chen, C. L.; Huang, D. X.; Lin, Y.; Chen, X.; Jacobson, A. J. High Temperature Electrical Conductivity of Epitaxial Gd-Doped CeO_2 Thin Films. *Solid State Ionics* **2004**, *175*, 103–106.

27. Chen, L.; Chen, C. L.; Chen, X.; Donner, W.; Liu, S. W.; Lin, Y.; Huang, D. X.; Jacobson, A. J. Electrical Properties of a Highly Oriented, Textured Thin Film of the Ionic Conductor Gd: $CeO_{2-\delta}$ on (001) MgO. *Appl. Phys. Lett.* **2003**, *83*, 4737–4739.

28. Hytch, M. J.; Snoeck, E.; Kilaas, R. Quantitative Measurement of Displacement and Strain Fields from HREM Micrographs. *Ultramicroscopy* **1998**, *74*, 131–146.

29. Hong, W. T.; Gadre, M.; Lee, Y. L.; Biegalski, M. D.; Christen, H. M.; Morgan, D.; Shao-Horn, Y. Tuning the Spin State in $LaCoO_3$ Thin Films for Enhanced High-Temperature Oxygen Electrocatalysis. *J. Phys. Chem. Lett.* **2013**, *4*, 2493–2499.

30. DeWolf, I. Micro-Raman Spectroscopy to Study Local Mechanical Stress in Silicon Integrated Circuits. *Semicond. Sci. Technol.* **1996**, *11*, 139–154.

31. Irmer, G.; Brumme, T.; Herms, M.; Wernicke, T.; Kneissl, M.; Weyers, M. Anisotropic Strain on Phonons in a-plane GaN Layers Studied by Raman Scattering. *J. Mater. Sci. Mater. Electron.* **2008**, *19*, S51–S57.

32. Huang, M. Y.; Yan, H. G.; Chen, C. Y.; Song, D. H.; Heinz, T. F.; Hone, J. Phonon Softening and Crystallographic Orientation of Strained Graphene Studied by Raman Spectroscopy. *Proc. Natl. Acad. Sci. U. S. A.* **2009**, *106*, 7304–7308.

33. Evans, A.; Bieberle-Hutter, A.; Galinski, H.; Rupp, J. L. M.; Ryll, T.; Scherrer, B.; Tolke, R.; Gauckler, L. J. Micro-Solid Oxide Fuel Cells: Status, Challenges, and Chances. *Monatsh. Chem.* **2009**, *140*, 975–983.

34. Evans, A.; Bieberle-Hutter, A.; Rupp, J. L. M.; Gauckler, L. J. Review on Microfabricated Micro-Solid Oxide Fuel Cell Membranes. *J. Power Sources* **2009**, *194*, 119–129.

35. Strukov, D. B.; Borghetti, J. L.; Williams, R. S. Coupled Ionic and Electronic Transport Model of Thin-Film Semiconductor Memristive Behavior. *Small* **2009**, *5*, 1058–1063.

36. Yang, J. J. S.; Strukov, D. B.; Stewart, D. R. Memristive Devices for Computing. *Nat. Nanotechnol.* **2013**, *8*, 13–24.

37. International Technoloy Roadmap for Semiconductor Industry (ITRS) 2011 Edition, Emerging Research Devices. http://www.itrs.net/, accessed February 14, 2014.

38. Waser, R.; Aono, M. Nanoionics-Based Resistive Switching Memories. *Nat. Mater.* **2007**, *6*, 833–840.

39. Waser, R.; Dittmann, R.; Staikov, G.; Szot, K. Redox-Based Resistive Switching Memories—Nanoionic Mechanisms, Prospects, and Challenges. *Adv. Mater.* **2009**, *21*, 2632–2663.

40. Sacchetto, D.; Gaillardon, P. E.; Zervas, M.; Carrara, S.; De Micheli, G.; Leblebici, Y. Applications of Multi-Terminal Memristive Devices: A Review. *IEEE Xplore: Circ. Syst. Mag.* **2013**, *13*, 23–41.

41. Linn, E.; Rosezin, R.; Tappertzhofen, S.; Bottger, U.; Waser, R. Beyond von Neumann-Logic Operations in Passive Crossbar Arrays Alongside Memory Operations. *Nanotechnology* **2012**, *23*, 305205.

42. Rosezin, R.; Linn, E.; Nielen, L.; Kugeler, C.; Bruchhaus, R.; Waser, R. Integrated Complementary Resistive Switches for Passive High-Density Nanocrossbar Arrays. *IEEE Electron Device Lett.* **2011**, *32*, 191–193.

43. Sacchetto, D.; De Micheli, G.; Leblebici, Y. Multiterminal Memristive Nanowire Devices for Logic and Memory Applications: A Review. *Proc. IEEE* **2012**, *100*, 2008–2020.

44. Dou, C.; Kakushima, K.; Ahmet, P.; Tsutsui, K.; Nishiyama, A.; Sugii, N.; Natori, K.; Hattori, T.; Iwai, H. Resistive Switching Behavior of a CeO$_2$ Based ReRAM Cell Incorporated with Si Buffer Layer. *Microelectron. Reliab.* **2012**, *52*, 688–691.

45. Liao, Z. L.; Chen, D. M. A Metal Oxide Heterostructure for Resistive Random Access Memory Devices. *Chin. Phys. Lett.* **2013**, *30*, 047701.

46. Liao, Z. L.; Gao, P.; Meng, Y.; Fu, W. Y.; Bai, X. D.; Zhao, H. W.; Chen, D. M. Electrode Engineering for Improving Resistive Switching Performance in Single Crystalline CeO$_2$ Thin Films. *Solid-State Electron.* **2012**, *72*, 4–7.

47. Lin, C. Y.; Lee, D. Y.; Wang, S. Y.; Lin, C. C.; Tseng, T. Y. Reproducible Resistive Switching Behavior in Sputtered CeO$_2$ Polycrystalline Films. *Surf. Coat. Technol.* **2008**, *203*, 480–483.

48. Sun, X.; Sun, B.; Liu, L. F.; Xu, N.; Liu, X. Y.; Han, R. Q.; Kang, J. F.; Xiong, G. C.; Ma, T. P. Resistive Switching in CeO$_x$ Films for Nonvolatile Memory Application. *IEEE Electron Device Lett.* **2009**, *30*, 334–336.

49. Zhu, Y. D.; Li, M. Y.; Zhou, H.; Hu, Z. Q.; Liu, X. L.; Liao, H. H. Improved Bipolar Resistive Switching Properties in CeO$_2$/ZnO Stacked Heterostructures. *Semicond. Sci. Technol.* **2013**, *28*, 015023.

50. Karageorgakis, N. I.; Heel, A.; Rupp, J. L. M.; Aguirre, M. H.; Graule, T.; Gauckler, L. J. Properties of Flame Sprayed Ce$_{0.8}$Gd$_{0.2}$O$_{1.9-\delta}$ Electrolyte Thin Films. *Adv. Funct. Mater.* **2011**, *21*, 532–539.

51. Rupp, J. L. M.; Scherrer, B.; Schauble, N.; Gauckler, L. J. Time-Temperature-Transformation (TTT) Diagrams for Crystallization of Metal Oxide Thin Films. *Adv. Funct. Mater.* **2010**, *20*, 2807–2814.

52. Brauer, G.; Gradinger, H. Uber Heterotype Mischphasen bei Seltenerdoxyden 0.2. Die Oxydsysteme des Cers und des Praseodyms. *Z. Anorg. Allg. Chem.* **1954**, *277*, 89–95.

53. Saiki, A. I. N.; Mizutani, N.; Kato, M. Structural Change of C-rare Earth Sesquioxides Yb$_2$O and Er$_2$O$_3$ as a Function of Temperature. *J. Ceram. Soc. Jpn.* **1985**, *93*, 649–654.

54. Schuller, I. K. New Class of Layered Materials. *Phys. Rev. Lett.* **1980**, *44*, 1597–1600.

55. Le Marrec, F.; Farhi, R.; El Marssi, M.; Dellis, J. L.; Karkut, M. G.; Ariosa, D. Ferroelectric PbTiO$_3$/BaTiO$_3$ Superlattices: Growth Anomalies and Confined Modes. *Phys. Rev. B: Condens. Matter Mater. Phys.* **2000**, *61*, R6447–R6450.

56. Dargis, R.; Williams, D.; Smith, R.; Arkun, E.; Roucka, R.; Clark, A.; Lebby, M. Structural and Thermal Properties of Single Crystalline Epitaxial Gd$_2$O$_3$ and Er$_2$O$_3$ Grown on Si(111). *ECS J. Solid State Sci. Technol.* **2012**, *1*, N24–N28.

57. Hong, S. J.; Virkar, A. V. Lattice-Parameters and Densities of Rare-Earth-Oxide Doped Ceria Electrolytes. *J. Am. Ceram. Soc.* **1995**, *78*, 433–439.

58. Jang, H. W.; Ortiz, D.; Baek, S. H.; Folkman, C. M.; Das, R. R.; Shafer, P.; Chen, Y.; Nelson, C. T.; Pan, X.; Ramesh, R.; *et al.* Domain Engineering for Enhanced Ferroelectric Properties of Epitaxial (001) BiFeO Thin Films. *Adv. Mater.* **2009**, *21*, 817–823.

59. Lejus, A. M.; Michel, D. Raman-Spectrum of Er$_2$O$_3$ Sesquioxide. *Phys. Status Solidi B* **1977**, *84*, K105–K108.

60. Gruber, J. B.; Chirico, R. D.; Westrum, E. F. Correlation of Spectral and Heat-Capacity Schottky Contributions for Dy$_2$O$_3$, Er$_2$O$_3$, and Yb$_2$O$_3$. *J. Chem. Phys.* **1982**, *76*, 4600–4605.

61. Muthukkumaran, K.; Kuppusami, P.; Kesavamoorthy, R.; Mathews, T.; Mohandas, E.; Raghunathan, V. S.; Selladurai, S. Microstructural Studies of Bulk and Thin Film GDC. *Ionics* **2008**, *14*, 165–171.

62. Kossoy, A.; Feldman, Y.; Korobko, R.; Wachtel, E.; Lubomirsky, I.; Maier, J. Influence of Point-Defect Reaction Kinetics on the Lattice Parameter of Ce$_{0.8}$Gd$_{0.2}$O$_{1.9}$. *Adv. Funct. Mater.* **2009**, *19*, 634–641.

63. Kreisel, J.; Weber, M. C.; Dix, N.; Sanchez, F.; Thomas, P. A.; Fontcuberta, J. Probing Individual Layers in Functional Oxide Multilayers by Wavelength-Dependent Raman Scattering. *Adv. Funct. Mater.* **2012**, *22*, 5044–5049.

64. Pikalova, E. Y.; Murashkina, A. A.; Maragou, V. I.; Demin, A. K.; Strekalovsky, V. N.; Tsiakaras, P. E. CeO$_2$ Based Materials Doped with Lanthanides for Applications in Intermediate Temperature Electrochemical Devices. *Int. J. Hydrogen Energy* **2011**, *36*, 6175–6183.

65. Korobko, R.; Chen, C. T.; Kim, S.; Cohen, S. R.; Wachtel, E.; Yavo, N.; Lubomirsky, I. Influence of Gd Content on the Room Temperature Mechanical Properties of Gd-Doped Ceria. *Scr. Mater.* **2012**, *66*, 155–158.

66. White, W. B.; Keramida, Vg. Vibrational-Spectra of Oxides with C-Type Rare-Earth Oxide Structure. *Spectrochim. Acta, Part A* **1972**, *A 28*, 501–509.

67. Mermoux, M.; Crisci, A.; Baillet, F.; Destefanis, V.; Rouchon, D.; Papon, A. M.; Hartmann, J. M. Strain in Epitaxial Si/SiGe Graded Buffer Structures Grown on Si(100), Si(110), and Si(111) Optically Evaluated by Polarized Raman Spectroscopy and Imaging. *J. Appl. Phys.* **2010**, *107*, 013512.

68. Kourouklis, G. A.; Jayaraman, A.; Espinosa, G. P. High-Pressure Raman-Study of Ceo$_2$ to 35 GPa and Pressure-Induced Phase-Transformation from the Fluorite Structure. *Phys. Rev. B: Condens. Matter Mater. Phys.* **1988**, *37*, 4250–4253.

69. Fan, X. F.; Case, E. D.; Yang, Q.; Nicholas, J. D. Room Temperature Elastic Properties of Gadolinia-Doped Ceria as a Function of Porosity. *Ceram. Int.* **2013**, *39*, 6877–6886.

70. Swaminathan, N.; Qu, J. Evaluation of Thermomechanical Properties of Non-Stoichiometric Gadolinium Doped Ceria Using Atomistic Simulations. *Model Simul. Mater. Sci. Eng.* **2009**, *17*, 045006.

71. Kossoy, A.; Feldman, Y.; Wachtel, E.; Lubomirsky, I.; Maier, J. Elasticity of Solids with a Large Concentration of Point Defects II. The Chemical Strain Effect in Ce$_{0.8}$Gd$_{0.2}$O$_{1.9}$. *Adv. Funct. Mater.* **2007**, *17*, 2393–2398.

72. Hohnke, D. K. Ionic-Conduction in Doped Oxides with the Fluorite Structure. *Solid State Ionics* **1981**, *5*, 531–534.

73. Ruiz-Trejo, E. The optical Band Gap of Gd-Doped CeO$_2$ Thin Films as Function of Temperature and Composition. *J. Phys. Chem. Solids* **2013**, *74*, 605–610.

74. Zhu, Y. Y.; Chen, S.; Xu, R.; Fang, Z. B.; Zhao, J. F.; Fan, Y. L.; Yang, X. J.; Jiang, Z. M. Band Offsets of Er$_2$O$_3$ Films Epitaxially Grown on Si Substrates. *Appl. Phys. Lett.* **2006**, *88*, 162909.

75. Adachi, G.; Imanaka, N.; Kang, Z. C. *Binary Rare Earth Oxides*; Kluwer Academic Publishers: Dordrecht, 2004; pp 111−133.

76. Rupp, J. L. M.; Infortuna, A.; Gauckler, L. J. Thermodynamic Stability of Gadolinia-Doped Ceria Thin Film Electrolytes for Micro-Solid Oxide Fuel Cells. *J. Am. Ceram. Soc.* **2007**, *90*, 1792–1797.

77. Minervini, L.; Zacate, M. O.; Grimes, R. W. Defect Cluster Formation in M$_2$O$_3$-Doped CeO$_2$. *Solid State Ionics* **1999**, *116*, 339–349.

78. Andersson, D. A.; Simak, S. I.; Skorodumova, N. V.; Abrikosov, I. A.; Johansson, B. Optimization of Ionic Conductivity in Doped Ceria. *Proc. Natl. Acad. Sci. U. S. A.* **2006**, *103*, 3518–3521.

79. Pietrucci, F.; Bernasconi, M.; Laio, A.; Parrinello, M. Vacancy-Vacancy Interaction and Oxygen Diffusion in Stabilized Cubic ZrO$_2$ from First Principles. *Phys. Rev. B: Condens. Matter Mater. Phys.* **2008**, *78*, 094301.

80. Hull, S.; Norberg, S. T.; Ahmed, I.; Eriksson, S. G.; Marrocchelli, D.; Madden, P. A. Oxygen Vacancy Ordering within Anion-Deficient Ceria. *J. Solid State Chem.* **2009**, *182*, 2815–2821.

81. Burbano, M.; Norberg, S. T.; Hull, S.; Eriksson, S. G.; Marrocchelli, D.; Madden, P. A.; Watson, G. W. Oxygen Vacancy Ordering and the Conductivity Maximum in Y$_2$O$_3$-Doped CeO$_2$. *Chem. Mater.* **2012**, *24*, 222–229.

82. Wang, B.; Cormack, A. N. Strain Modulation of Defect Structure in Gadolinia-Doped Ceria. *J. Phys. Chem. C* **2013**, *117*, 146–151.

83. De Souza, R. A.; Ramadan, A.; Horner, S. Modifying the Barriers for Oxygen-Vacancy Migration in Fluorite-Structured CeO_2 Electrolytes through Strain: a Computer Simulation Study. *Energy Environ. Sci.* **2012**, *5*, 5445–5453.

84. Hinterberg, J.; Zacherle, T.; De Souza, R. A. Activation Volume Tensor for Oxygen-Vacancy Migration in Strained CeO_2 Electrolytes. *Phys. Rev. Lett.* **2013**, *110*, 205901.

85. Perkins, J. M.; Fearn, S.; Cook, S. N.; Srinivasan, R.; Rouleau, C. M.; Christen, H. M.; West, G. D.; Morris, R. J. H.; Fraser, H. L.; Skinner, S. J.; *et al.* Anomalous Oxidation States in Multilayers for Fuel Cell Applications. *Adv. Funct. Mater.* **2010**, *20*, 2664–2674.